Characterizing water-soluble Bbrown carbon in fine particles in four typical cities in Northwest China during wintertime: coupling Integrating optical properties with chemical processes

Miao Zhong[a,b], Jianzhong Xu[a,*], Huiqin Wang[c], Li Gao[d], Haixia Zhu[e], Lixiang Zhai[a,b], Xinghua Zhang[a], Wenhui Zhao[a,b]

[a]State Key Laboratory of Cryospheric Sciences, Northwest Institute of Eco-Environment and Resources, Chinese Academy of Sciences, Lanzhou 730000, China
[b]University of Chinese Academy of Sciences, Beijing 100049, China
[c]Institute of Desert Meteorology, China Meteorological Administration, Urumqi 830002, China
[d]School of Geography and Planning, Ningxia University, Yinchuan 750021, ChinaCollege of Resources and Environment, Ningxia University, Yinchuan 750021, China
[e]Key Laboratory of Comprehensive and Highly Efficient Utilization of Salt Lake Resources, Qinghai Institute of Salt Lakes, Chinese Academy of Science, Xining, Qinghai 810008, China

* Corresponding author: Jianzhong Xu (jzxu@lzb.ac.cn)

Abstract

Brown carbon (BrC) aerosol could impact atmospheric radiative forcing and play a crucial role in atmospheric photochemistry. ~~Most previous studies have predominantly focused on bulk optical properties of ambient BrC from biomass burning emitted primary or secondary BrC aerosol. Few studies have focused on fossil-fuel-influenced BrC aerosol, especially coal combustion emissions.~~ In this study, fine particulate matter ($PM_{2.5}$) filter samples were collected synchronously in four capital cities of Northwest China during the winter season (December 2019–January 2020): Lanzhou (LZ), Xining (XN), Yinchuan (YC), and Urumqi (UR), which are represented as energy-producing and heavy manufacturing cities in China. The primary aim of the study is to explore the optical properties, sources, and chemical processes of water-soluble BrC (WS-BrC). The average mass absorption efficiency at 365 nm (MAE_{365}) of WS-BrC at these four cities was 1.24 ± 0.19 m^2/g (XN), 1.19 ± 0.12 m^2/g (LZ), 1.07 ± 0.23 m^2/g (YC), and 0.78 ± 0.16 m^2/g (UR), respectively. The properties of WS-BrC were further investigated by an acid-base titration experiment. The results showed that the MAE_{365} values in all cities increased with higher pH values (2–11), while the fluorescent intensities of water extracts fluctuated with pH values, being stronger under both highly acidic and basic conditions. The sensitivity to pH variation was most pronounced in the WS-BrC samples from YC and LZ, indicating the important contribution of acid/base functional group compounds in these locations. Additionally, the study revealed significant photo-enhancement (LZ) or photo-bleaching (YC and UR) phenomena of WS-BrC in different cities. These results suggest that the sources and/or chemical processes of WS-BrC varied among the cities.

The sources and chemical processes of WS-BrC were further explored by a combination of parallel factor analysis (PARAFAC) on excitation-emission matrix (EEM) spectra of WS-BrC and positive matrix factorization analysis (PMF) on high-resolution mass spectra of water-soluble organic aerosol (OA). Six PARAFAC components were

identified, including three humic-like substances (two LO-HULIS and one HO-HULIS~~LO-HULIS, HO-HULIS1, and HO-HULIS2~~), two protein-like (PLS) or phenol-like substances, and one undefined substance. Four PMF factors were identified, including a water-soluble primary OA (WS-POA), a less oxidized oxygenated OA associated with coal combustion-induced WSOA (LO-OOA), and two highly oxidized oxygenated OAs resulting from photochemical oxidation and aqueous-phase oxidation transformations (HO-OOA1 and HO-OOA2). WS-POA was determined to be the most significant source of light absorption, accounting for 30%–60% based on multiple linear regression models, and it showed a significant correlation with PLS and LO-HULIS components. The loss of light absorption of WS-POA was found to occur through its conversion to LO-OOA and HO-OOAs through photochemical or aqueous reactions, with HO-OOAs being significantly correlated with the HO-HULIS component. These processes can be clearly illustrated by integrating optical properties and chemical composition using Van Krevelen diagram and EEM plot.

Keywords: Brown carbon, AAE, fluorescent chromophores, HR-AMS, PMF

1. Introduction

Brown carbon (BrC) is a certain fraction of organic aerosols that absorb lights in the ultraviolet and visible (UV−Vis) ranges (Andreae and Gelencsér, 2006; Laskin et al., 2015). The light absorption of BrC displays a strong wavelength-dependence which can be characterized by higher value (≥ 2) of the absorption Ångström exponent (AAE) (Laskin et al., 2015). The significant effects of BrC on climate and atmospheric chemistry have been characterized previously. Wang et al. (2018) estimate the global mean absorption direct radiative effect (DRE) of BrC is +0.048W/m^2 using the GEOS-Chem chemical transport model. The absorption of solar radiation due to BrC can also affect the formation of ozone and radicals of •OH/•HO$_2$ and corresponding atmospheric chemical reactions (Mok et al., 2016; Baylon et al., 2018).

Biomass combustion is a major global source of primary BrC, as biomass is widely used for residential heating and cooking and is also produced during wildfires (Washenfelder et al., 2015; Lin et al., 2017; Zeng et al., 2020). Coal combustion is another important source of primary BrC, particularly in urban areas during the winter heating period (Tan et al., 2016; Hu et al., 2020; Yuan et al., 2021; Deng et al., 2022). In addition to primary sources, secondary BrC is formed through various reaction pathways related to biomass burning, such as aqueous oxidation of phenolic compounds or gas-phase photo-oxidation of aromatic volatile organic compounds (VOCs) (Lin et al., 2015; Vidovic et al., 2018; Liu et al., 2019; Vidovic et al., 2020)., such as gas-phase photo-oxidation of aromatic volatile organic compounds (VOCs), and nighttime aqueous-phase formation of aromatic nitration products in the atmospheric condensed phase (Lin et al., 2015; Vidovic et al., 2018; Liu et al., 2019). The chemical compositions and light absorption of BrC can vary significantly due to atmospheric aging. For instance, BrC can photobleaching through photolysis reactions in the presence of •OH radical and O$_3$, or darken via the formation of nitrated organic compounds (Lin et al., 2015;

Zhao et al., 2015; Moise et al., 2015; Li et al., 2020a). Furthermore, atmospheric conditions such as changes in pH, air temperature, and relative humidity can affect the light absorption characteristics of BrC (Song et al., 2013; Moise et al., 2015; Phillips et al., 2017; Qin et al., 2020).

The solvent extracts from filter samples have been widely used to assess the absorbing properties of BrC (Zhang et al., 2017; Wu et al., 2019; Xu et al., 2020b; Zou et al., 2023). Water-soluble BrC is only a portion of BrC, which accounts for approximately half of the total light absorption by solvent-extractable organic aerosols in urban areas (Cheng et al., 2017; Huang et al., 2018; Chen et al., 2020b), and exceeds half and even up to 90% in remote areas (Zhu et al., 2018; Li et al., 2022). ~~Various optical instruments are used to determine the light absorption of BrC. These instruments include direct measurement of airborne aerosol (e.g., particle soot absorption photometer, photoacoustic spectroscopy, and cavity ring-down spectroscopy) (Laskin et al., 2015) or offline measurement of aerosol extracts by UV-Vis spectrometer~~ The aerosol extracts are measured offline using a UV-Vis spectrometer to determine the light absorption of BrC (Hecobian et al., 2010). Excitation-emission matrix spectroscopy (EEMs) was recently used to reveal similar chemical structures and photochemical features, as well as to trace the sources of BrC chromophores (Chen et al., 2016; Tang et al., 2020). A few recent studies have characterized BrC compounds by combining high-resolution mass spectrometry and UV-vis spectroscopy (Lin et al., 2017; Wang et al., 2019; Huang et al., 2020; Ni et al., 2021), which facilitates the assessment of the chemical composition of BrC chromophores at the molecular level. Recent studies have identified the major water-soluble BrC species, including humic-like substances, phenols, nitroaromatics, and oxygenated aromatics (Cai et al., 2020; Qin et al., 2022a; Jiang et al., 2022; Zhou et al., 2022).

~~In China, coal is still a primary source of energy due to its extensive use in coal-fired~~

120 ~~power plants, industrial steam boilers, and central heating during winter. It is particu-~~
121 ~~larly prevalent in Western China, where numerous industrial bases have been estab-~~
122 ~~lished since the Development of China's Western Regions strategy in the 2000s.~~ In re-
123 cent years, cities in Northwest China have experienced more severe air pollution due to
124 rapid economic development and intensive anthropogenic activities, especially in the
125 capital cities of this region. ~~Some recent studies have identified coal combustion as a~~
126 ~~significant source of BrC in Northwest China (Tan et al., 2016; Chen et al., 2021; Zhang~~
127 ~~et al., 2021a). Compared with BrC resulting from biomass burning, the optical and~~
128 ~~chemical properties of BrC emitted from coal combustion have not been well-charac-~~
129 ~~terized.~~ Despite previous research on the chemical compositions and source apportion-
130 ment of atmospheric aerosols (Xu et al., 2014; Xu et al., 2016; Tan et al., 2016; Xu et
131 al., 2020a; Zhang et al., 2021a), the current understanding of the optical properties and
132 formation mechanisms of brown carbon over Northwest China is quite limited and de-
133 serves more attention. This study aims to characterize the optical properties of water-
134 soluble BrC (WS-BrC) by collecting $PM_{2.5}$ filter samples from four capital cities in
135 Northwest China and analyzing them using a suite of instruments. In particular, the
136 study focused on the contribution of primary and secondary sources of atmospheric
137 water-soluble chromophores and the related chemical processes. This objective could
138 be accomplished by combining data from Excitation-Emission Matrices Spectroscopy
139 (EEMs) and High-Resolution Aerosol Mass Spectrometry (HR-AMS).
140
141 **2. Methods**
142
143 2.1. Filter samples collection at the four cities
144
145 $PM_{2.5}$ filter samples were collected synchronously from four capital cities in Northwest
146 China, namely Yinchuan (YC), Xining (XN), Urumqi (UR), and Lanzhou (LZ), from
147 5th December 2019 to 20th January 2020 (Figure 1). The sampling sites were located
148 on building rooftops and situated within the cultural and educational districts of each

149 city, away from significant pollution sources. Filter samples were collected by a mid-

150 volume $PM_{2.5}$ sampler (Laoying Ltd., model 2030) with a flow rate of 100 L/min in YC

151 (sample IDs: 1−14), by a low-volume PM~~2.5~~$_{2.5}$ sampler (Wuhan Tianhong Instrument

152 Co Ltd., TH-16E) with a flow rate of 16.7 L/min in XN and UR (sample IDs: 15−28

153 and IDs: 29–42), and by a low-volume aerosol sampler (BGI, model PQ 200) with a

154 flow rate of 16.7 L/min in LZ (sample IDs: 43−56). Fine particles were collected onto

155 quartz filters with a 90-nm diameter (Whatman, UK) in YC and with a 45-nm diameter

156 (PALL Life Sciences, USA) in other cities, which had pre-baked at 550 °C for five

157 hours to eliminate carbonaceous particles. Blank filter samples were obtained from each

158 site by leaving the filters in the sampler for ten minutes without sampling. Each filter

159 was wrapped in aluminum foil and frozen at −20 °C until analysis. The daily average

160 concentration of $PM_{2.5}$, SO_2, NO_2, CO, O_3, and meteorological data (air temperature

161 and relative humidity) were obtained from the nearest station of the National Environ-

162 mental Monitoring Net sites (http://www.cnemc.cn/) for comparison. Figure 1 also il-

163 lustrates the energy consumption structure of industrial enterprises in four cities, with

164 YC, UR, and LZ being energy production cities, and XN being a heavy manufacturing

165 city (Shan et al., 2018). The energy consumption data for 2019 was obtained from the

166 Statistical Yearbook sharing platform (https://www.yearbookchina.com/).

167

168 2.2. Chemical analysis

169

170 The chemical components of the samples were analyzed using multiple instruments.

171 Firstly, a piece of each filter ($0.50 cm^2$) was analyzed for organic carbon (OC) and ele-

172 mental carbon (EC) contents using a Thermal/Optical carbon analyzer (DRI Model

173 2015A, Desert Research Institute, USA) with the IMPROVE-A method (Chow et al.,

174 2007). One-quarter of each filter from YC and half of each filter from other cities were

175 extracted in 30ml of Milli-Q water (18.2 M Ω·cm) using an ultrasonic bath for 40

176 minutes. Ice was added to the ultrasonic bath to minimize chemical reactions and evap-

177 oration loss during sonication. Water-insoluble residuals were eliminated by filtering

extracts via a 0.45-μm PTFE syringe filter (Pall Life Sciences, USA). The concentra-

tions of water-soluble inorganic ions (WSIIs) (Cl$^-$, NO$_3^-$, SO$_4^{2-}$, NH$_4^+$, Na$^+$, K$^+$, Ca^{2+},

and Mg^{2+}) were analyzed using two 881 compact ion chromatography systems

(Metrohm, Herisau, Switzerland). The operation details can be found elsewhere (Xu et

al., 2015). WSOC was analyzed using a TOC analyzer (Elementar Vario TOC cube,

Hanau, Germany) with the method of total inorganic carbon (TIC) subtracted from total

carbon (TC) (Xu et al., 2015; Zhang et al., 2017).

2.3. Analysis by ultraviolet-visible absorption spectroscopy

2.3. Analysis by ultraviolet-visible absorption spectroscopy

The absorption spectra of water extracts in the 200–700 nm wavelength range were

obtained using a UV-visible absorption spectrophotometer (UV-2700; Shimadzu,

Kyoto, Japan) at 1 nm intervals with Milli-Q water as the reference. The absorption

spectra were corrected by subtracting the average absorbance between 690–700 nm

(A_{700}) from the absorbance at wavelength λ.

The light absorption coefficient at a given wavelength (Abs_λ, M/m) of water extracts is

calculated as follows:

$$Abs_\lambda = (A_\lambda - A_{700}) \times \frac{V_l}{V_a \cdot l} \times \ln(10) \tag{1}$$

where A_λ is the absorbance at wavelength λ; V_l is the extract volume (30 mL), V_a is

the volume of air passing through the filter, and l is the optical path length, 5 cm.

The mass absorption efficiency (MAE_λ, m^2/g) of water extracts can be derived as

follows:

$$MAE_\lambda = \frac{Abs_\lambda}{C_{WSOC}} \tag{2}$$

205   where C_{WSOC} represents the mass concentration of WSOC in the extract. For simplic-

206   ity, the absorption at 360–370 nm (mean 365 nm) is used to characterize the absorption

207   of BrC (Hecobian et al., 2010).

208

209   The spectral dependence of light absorption fits a power law as follows:

210 $$Abs_\lambda = K \cdot \lambda^{-AAE} \tag{3}$$

211   where K is a constant related to light absorption, and the absorption Ångström exponent

212   (AAE) can be fitted at the range of 300–400 nm.

213

214   The imaginary part k of the particle refractive index represents the light absorption by

215   aerosols and can be calculated as follows (Liu et al., 2013):

216 $$k_\lambda = \frac{MAE_\lambda \times \lambda \times \rho}{4\pi} \tag{4}$$

217   where ρ (g/cm^3) is estimated as $\rho = (12 + H/C + 16 \times O/C) / (7 + 5 \times H/C + 4.15 \times O/C)$

218   (Kuwata et al., 2012).

219

220   The direct radiative forcing of WS-BrC is estimated by the simple forcing efficiency

221   model (SFE). The wavelength-dependent SFE$_{Abs}$ (W/g) of WS-BrC is calculated using

222   the following equation (Bikkina and Sarin, 2019):

223 $$\frac{dSFE_{Abs}}{d\lambda} = D\frac{dS(\lambda)}{d\lambda}\tau_{atm}^2(1 - F_C) \times 2\alpha_S \times MAE_\lambda \tag{5}$$

224   where $S(\lambda)$ represents the wavelength-dependent solar irradiance, obtained from ASTM

225   G173–03 reference spectra. Additionally, τ_{atm} refers to atmospheric transmission (0.79);

226   D is assigned the value of 0.5, representing the proportion of daylight hours; F_C is set

227   to 0.6, representing the cloud proportion; α_s is fixed at 0.19 for the global average, rep-

228   resenting the surface albedo (Chen and Bond, 2010).

229

230   2.4. EEM fluorescence spectra analysis

231

232   The three-dimensional excitation-emission matrix spectroscopy (EEMs) of the samples

233   were obtained using an F-7100 fluorescence spectrometer (Hitachi High-Technologies,

Japan). The EEMs were measured in the range of 200 to 400 nm with 5 nm intervals for excitation and 250 to 550 nm with 1 nm intervals for emission. The inner filter effect was reduced by diluting the extracts until their absorbance was below 0.1 at 254 nm (Ohno, 2002). The original EEMs were processed following: (1) subtracting the Milli-Q water spectrum to reduce background influence, (2) interpolating to eliminate the interference signals of the Rayleigh scattered light, then (3) adjusting the fluorescence intensity by dividing the Raman peak area of Milli-Q water at Ex = 350 nm to remove instrument dependency (Lawaetz and Stedmon, 2009).

The obtained fluorescence intensities (unit of RU) were further processed using parallel factor analysis (PARAFAC) to group potentially similar chemical components. This process was conducted using the MATLAB 2016b software combined with the DOM-Fluor and drEEM toolboxes (Murphy et al., 2013). The 6-component model was eventually chosen from 2- to 10-component PARAFAC models because the residual errors decreased markedly when the number of components increased from 2 to 6 (Figure S1). In addition, the 6-component model has reasonable spectra of each fluorescent component.

Furthermore, the fluorescence properties of the water extracts were examined through the fluorescence indices. The humification index (HIX) was calculated by the ratio of the integrated fluorescence emission intensity in the region of 435–480 nm to 300–345 nm under the excitation wavelength of 255 nm. The biological index (BIX) was calculated by the ratio of the emission intensity of 380 nm to 430 nm under the excitation wavelength of 310 nm (Zsolnay et al., 1999; Mcknight et al., 2001; Yang et al., 2020b). The average fluorescence intensities (AFI) can be calculated in the region of 200–400 nm for excitation wavelengths and 250–550 nm for emission wavelengths.

The apparent fluorescence quantum yields (AQY) can be calculated as follows:

$$AQY_\lambda = \frac{\int FI(\lambda_{Ex},\ \lambda_{Em})d\lambda_{Em}}{UVA(\lambda_{Ex})\int d\lambda_{Em}}\bigg|_{Ex} \tag{6}$$

where FI represents the fluorescence intensity (RU) at each excitation (200–400 nm) and emission (250–550 nm) wavelength.

2.5. pH titration experiment

To investigate the variation of light-absorbing and fluorescent properties of ambient aerosols under the influence of pH, we selected samples with higher WSOA concentrations at each city and recorded their UV-vis absorption and fluorescence spectra at different pH settings. The water extracts were adjusted to pH 2 using 2 M HCl and then titrated with 0.1 M NaOH to different pH values until the pH reached 11, as measured by a pH meter (Orion Star A111, Thermo Fisher Scientific, Waltham, MA, USA). The pH meter was calibrated with buffer solutions of pH 4.01, 7.00, and 10.01 during the measurement.

2.6. HR-AMS Measurements

Offline measurements by high-resolution time-of-flight aerosol mass spectrometry (HR-AMS) were conducted to analyze the ion group, elemental ratio, and oxidation properties of water-soluble organic aerosol (WSOA). Each sample was atomized with argon (purity: 99.9999%) to eliminate interference from CO_2 in the air. The generated aerosol was passed through a silica gel diffusion dryer to remove water vapors, and the aerosol particles were then sampled into an HR-AMS instrument (Aerodyne Inc., Billerica, MA, USA) through an aerodynamic lens inlet. The HR-AMS was operated in both V- and W-mode. Deionized water was aerosolized and analyzed in the same procedures between every two samples. Elemental ratios, including O/C, H/C, N/C, and OM/OC, were determined based on high-resolution mass spectra (m/z up to 120) and the Improved-Aiken (I-A) method (Canagaratna et al., 2015). The elemental contributions of C, O, H, and N reported are mass-based, and more details can be found elsewhere (Xu et al., 2013). Positive matrix factorization (PMF) was performed on high-

292 resolution mass spectra of WSOA at four cities to identify the potential source factors

293 of WSOA, and four factors were ultimately decomposed. A detailed description of PMF

294 can be found in Zhao et al. (2022).

295

296 In addition, the mass concentration of WSOA can be calculated as follows:

297 $$WSOA = WSOC \times (OM/OC) \qquad\qquad (7)$$

298

299 **3. Results and discussions**

300

301 3.1. Overview of the field observations

302

303 Figure 2 presents an overview of the time series of meteorological conditions (air tem-

304 perature, relative humidity (RH), and precipitation), Abs_{365}, AFI, as well as the mass

305 concentrations of ~~WSIs~~WSIIs, WSOA, and EC in the four cities. The weather during

306 the study was generally sunny, cold, and dry (Figure 2a). For instance, the average (±

307 1σ) daily air temperature was –3.2 ± 3.4 °C at YC, –4.4 ± 2.2 °C at XN, –9.2 ± 3.7 °C

308 at UR, and –3.8 ± 2.5 °C at LZ, respectively, and the average (± 1σ) RH was 62.4 ±

309 15.8% at YC, 56.1 ± 14.7% at XN, and 58.1 ± 9.7% at LZ. At UR, there were relatively

310 higher RH conditions (83.9 ± 6.6%), and frequent foggy weather and two snowfall

311 events were observed mainly due to the invasion of cold and wet air mass from the

312 Arctic Ocean during winter (Yang et al., 2020a). Both the cold/wet and cold/dry weather

313 conditions in our study facilitated the study of different chemical processes.

314

315 The mass concentrations of chemical species of $PM_{2.5}$, as well as their mass fractions,

316 varied dynamically during the sampling period in four cities (Figure 2c and 2d). Heavy

317 pollution (the daily average $PM_{2.5}$ mass concentration higher than 150 ~~$\mu g\ m^{-3}$~~ $\mu g/m^3$)

318 occurred frequently in UR, followed by YC (Figure 1). These heavy pollution events,

319 such as the sample ID of 10–13 and 36–40, commonly occurred under high RH condi-

320 tions (Figures 2a and 2c), which were favorable for the secondary generation of atmos-

321 pheric particulate matter (Sun et al., 2013). Therefore, the contribution of secondary

322 inorganic ions (SNA: sulfate + nitrate + ammonium) showed an important contribution

323 to the reconstructed $PM_{2.5}$ mass (WSOA + EC + ~~WSIs~~WSIIs) with an average of 53.0

324 ± 12.7%, 41.6 ± 11.5%, 67.3 ± 7.8%, and 41.8 ± 7.3%, respectively, in YC, XN, UR,

325 and LZ, and could be as high as 65.6–76.9% during heavy pollution period at YC and

326 UR (Figure 2d). WSOA was also a major component of $PM_{2.5}$ accounting for 31.4 ±

327 5.5%, 40.6 ± 5.4%, 21.8 ± 4.6%, and 37.7 ± 4.1% at YC, XN, UR, and LZ, respectively.

328 The mass contribution of EC was comparable in four cities (5.8–8.9%). The higher

329 contribution of SNA at YC and UR, in contrast with the higher contribution of WSOA

330 at XN and LZ, likely suggested their different sources and chemical processes. The

331 contributions of WSOA and SNA at XN and LZ in our study were comparable with

332 those in Xi'an, another megacity in Northwest China, during wintertime (Huang et al.,

333 2014), while YC and UR showed greater similarity with cities in East China, such as

334 Beijing, Tianjin, and Jinan, where relatively wet condition during wintertime (Lei et al.,

335 2021; Zhang et al., 2021c; Dao et al., 2022).

336

337 The ratio of WSOC/OC is commonly used to predict the potential contribution of sec-

338 ondary organic aerosol to total organic aerosol (Psichoudaki and Pandis, 2013). Overall,

339 WSOC showed a strong correlation with OC (R^2 = 0.84) with a linear slope of 0.55 for

340 all samples from four cities (Figure S3). The slope values varied among the cities, with

341 YC and UR having higher values (0.61 and 0.59) than XN and LZ (0.54 and 0.52),

342 suggesting a potentially higher secondary OA formation in YC and UR. The WSOC/OC

343 values in our study were within the range reported in other cities during winter, such as

344 Xi'an (0.50 and 0.53) (Zhang et al., 2018; Liu et al., 2020), Beijing (0.~~74~~54) (Ni et al.,

345 2022), and Guangzhou (0.~~71~~55) (Tao et al., 2022). Significant correlations among cor-

346 relations among WSOC, OC, EC, Cl⁻, K⁺ and SNA were found in four cities, indicating

347 the primary and secondary sources of water-soluble organic compounds (Figure S2,

348 Table S3). Furthermore, the Abs_{365} and AFI values varied with WSOC concentration,

349 and we observed significant correlation between them ($R^2_{\text{Abs Vs. WSOC}} = 0.87$; $R^2_{\text{AFI Vs.}}$

350 $_{\text{WSOC}} = 0.61$). These findings suggest indicating an important contribution of WS-BrC

351 chromophores to WSOC.

352

353

354 3.2. Bulk optical properties of WS-BrC

355

356 Figure 3a presents the average MAE spectra of WSOA from various cities. XN and LZ

357 exhibited significantly higher MAE_{365} values (on average 1.22 ± 0.18 and 1.19 ± 0.12

358 m^2/g) compared to YC (1.02 ± 0.23 m^2/g) and UR (0.78 ± 0.16 m^2/g) (t-test, P < 0.01)

359 (Table 1). When compared with previous studies in wintertime, the MAE_{365} in XN and

360 LZ were comparable to those of Beijing (1.21–1.26) (Du et al., 2014; Cheng et al., 2016;

361 Li et al., 2020b), the MAE_{365} in YC were close to those of southern cities in China, such

362 as Guangzhou (0.93 ± 0.06 m^2/g), Nanjing (1.04 m^2/g) (Fan et al., 2016; Chen et al.,

363 2018), the MAE_{365} in UR was similar to that of Yangzhou (0.75 ± 0.29 m^2/g) (Chen et

364 al., 2020b). In addition, the imaginary refractive index at 365 nm (k_{365}) for WS-BrC

365 showed the same trend as MAE_{365}, i.e., XN (0.034 ± 0.007) > LZ (0.031 ± 0.007) > YC

366 (0.029 ± 0.009) > UR (0.023 ± 0.007) (Table 1). Overall, the k_{365} values in this study

367 were comparable to those reported in other urban areas, such as Kanpur in central India

368 during winter (0.042) (Choudhary et al., 2021) and Jinan in northern China during

369 spring (0.035) (Wen et al., 2021); however, they were higher than those reported in the

370 Himalayan cryosphere during winter (0.009–0.026) (Choudhary et al., 2022) and in the

371 northeast margin of Qinghai-Tibetan Plateau during summer (0.022) (Xu et al., 2020b).

372 Previous studies indicated that photochemical aging decreased the k values for BrC

373 aerosols (Laskin et al., 2015; Sumlin et al., 2017).

374

375 AAE denotes the wavelength dependence of light absorption of BrC, an important op-

376 tical parameter that can be used to infer the chemical properties of BrC (Andreae and

377 Gelencsér, 2006). In this study, the AAE values at YC, XN, and UR were 6.8 ± 0.7, 7.1

± 0.4, and 6.9 ± 0.3, respectively. Significantly lower AAE was observed (6.4 ± 0.5) at LZ (t-test, P < 0.01) (Table 1). Our AAE values fell within the range of values reported in other cities during winter for $PM_{2.5}$ water extracts calculated in the same wavelength range, such as at Nanjing (6.8) (Chen et al., 2018), Beijing (7.3 and 7.5) (Du et al., 2014; Cheng et al., 2016), and Guangzhou (6.7 ± 0.1) (Fan et al., 2016). Previous studies have suggested that higher AAE values may be associated with primary biomass combustion emissions and/or SOA formation. For instance, Chen and Bond (2010) emphasized that particles from smoldering of various wood have higher values of 7–16. Lambe et al. (2013) indicated that secondary BrC generated in the laboratory also has a higher AAE value (5.2–8.8). Therefore, the differences in AAE values among the four cities may indicate their different sources or/and chemical compositions.

Saleh (2020) proposed an optical-based classification of BrC using the space of MAE_{405} vs. AAE, which is linked with their physicochemical properties (i.e., molecular sizes and solubility) and atmospheric aging (i.e., photo-enhancement or photo-bleaching). Almost all samples in this study fell into the region of W-BrC (Weakly absorptive BrC), which is similar to ambient samples from other studies (Zhou et al., 2021; Xu et al., 2022). However, a few samples at UR fell into the region of VW-BrC (Very weakly absorptive BrC). Furthermore, the WS-BrC in YC exhibited a broader range than other cities, indicating multiple sources and/or processes for WS-BrC in this city. Higher AAE and MAE_{405} values were found in XN, which could be associated with biomass burning emissions. Additionally, WS-BrC in LZ was the closest to the region of M-BrC (Moderately absorptive BrC) among the four cities, and the different positions could be related to their chemical processes in each city. For instance, upon examining the relationship between MAE_{365} and the O/C ratio, a positive correlation was observed only in LZ, while negative relationships were observed in other cities (Figure 10). The chemical processes of WS-BrC are discussed in detail in section 3.7.

We estimated the integrated mean SFE values of WS-BrC within the 300–700 nm range

 (SFE$_{300-700}$) due to the abrupt decrease of solar spectral energy below 300 nm and the

 negligible absorption of solar radiation by BrC above 700 nm. SFE$_{300-700}$ was larger at

 XN (4.42 ± 0.72 W/g) and LZ (4.35 ± 1.01W/g) than at YC (3.72 ± 0.90 W/g) and UR

 (2.97 ± 0.6 W/g) (Table 1), indicating their stronger light-absorbing capacity of WS-

 BrC. The SFE values in this study were similar to those in Hong Kong during winter

 (4.4 W/g) (Zhang et al., 2020), slightly higher than those in Jinan during spring (3.3

 W/g) (Wen et al., 2021), but only half of those in laboratory biomass burning samples

 (7.7–8.3 W/g) (Lei et al., 2018).

 3.3. Fluorescence Indices

 Fluorescence indexes, such as HIX and BIX, have been used in recent years to study

 the source and chemical processes of atmospheric organic aerosols (Lee et al., 2013; Fu

 et al., 2015; Qin et al., 2018; Deng et al., 2022). The HIX indicates the degree of

 humification of WSOA, and it increases significantly upon aging (Lee et al., 2013; Fan

 et al., 2020). The BIX is broadly in contrast with HIX and is known as the freshness

 index. A higher BIX value implies a higher contribution of freshly released organics,

 while a lower value indicates greater degrees of aging (Lee et al., 2013; Wen et al.,

 2021).

 Table 1 shows that the HIX and BIX values were 1.85 ± 0.36 and 1.28 ± 0.14 at UR,

 1.32 ± 0.23 and 1.48 ± 0.11 at YC, 1.29 ± 0.27 and 1.49 ± 0.15 at XN, and 1.16 ± 0.18

 and 1.52 ± 0.11at LZ, respectively. The highest HIX value and lowest BIX value were

 found in UR, indicating a higher degree of aging/oxidation of WS-BrC. On the other

 hand, the lower HIX and higher BIX values observed in LZ suggest a high contribution

 of freshly emitted BrC. These results were consistent with the results of the MAE$_{365}$

 discussed earlier.

 The HIX exhibites a significant negative correlation with BIX across all the data ($R^2 =$

436   0.86, slope = 2.19) (Figure 4a). In Figure 4b, a comparison is presented between our

437   findings and other datasets derived from laboratory or ambient aerosols in different

438   cities throughout China. These datasets can be roughly categorized into three zones,

439   distinguished by the gray, pink, and blue dashed boxes. The freshly introduced materials

440   generated from the laboratory (gray box) were located at a much lower position than

441   those of ambient samples. Differences also existed in ambient samples, with higher

442   (lower) BIX (HIX) values from our samples (pink box) than those from Eastern China

443   (blue box) (Qin et al., 2018; Yue et al., 2019; Wen et al., 2021; Deng et al., 2022), which

444   suggested that our samples are generally less aged than those from Eastern cities,

445   although the position of UR fell within the overlapped range between these two zones.

446

447   3.4. Influence of pH on optical properties

448

449   Recent studies have shown that the optical properties of BrC vary depending on pH,

450   which is important for modeling its climate-forcing effect, as the general assumption of

451   a neutral state for aerosol in models may not be accurate (Phillips et al., 2017). We

452   investigated the effect of pH on the absorption and fluorescence spectra of WSOA for

453   our samples (Figures 5 and 6). The absorption spectra showed a significant increase in

454   absorbance with the increasing pH values (from 2 to 10)~~, with the integrated absorbance~~

455   ~~(300–450 nm) increased by 66.6%, 55.2%, 43.4%, and 25.3% relative to the pH = 2~~

456   ~~level, respectively, in YC, LZ, XN, and UR (Figure S4)~~. The integrated absorbance

457   (300–450 nm) increased by 66.6%, 55.2%, 43.4%, and 25.3% in YC, LZ, XN, and UR

458   at pH 10 relative to pH 2 (Figure S4). The MAE_{365} increased with increasing pH values

459   (slope = 0.03–0.07), while the AAE decreased (slope = –0.15 to –0.40) (Figure S5).

460   Notably, the light absorption spectra in YC and LZ exhibited greater sensitivity to pH

461   variation, evident from their steeper slopes. Previous studies have observed variations

462   in light absorbance as a function of pH, attributing these changes to the

463   protonation/deprotonation of carboxyl/phenolic functional groups and/or alterations in

464   macromolecular conformation (Lin et al., 2017; Phillips et al., 2017; Xu et al., 2020b;

465 Qin et al., 2020; Qin et al., 2022a). The different sensitivity of WS-BrC to pH at our

466 sampling sites suggested variations in chemical compositions among them, which could

467 be further investigated through fluorescence spectra.

468

469 The EEM spectra exhibited the highest fluorescent intensity values at pH = 2 and tended

470 to decrease with increasing pH. However, for the YC and UR samples, the fluorescent

471 intensity at pH = 10 slightly increased compared to that at pH = 7 (Figure 6). The

472 underlying mechanism behind the variations in fluorescence intensity with pH values

473 may be related to the rigid properties of fluorophores. Specifically, the formation of

474 hydrogen bonds at lower pH values could give the aggregates a stronger rigid planar

475 conformation and enhance fluorescence efficiency (Ghosh and Schnitzer, 1981; Mei et

476 al., 2009). As pH values increased, the repulsion among generated anions disrupts

477 hydrogen bonding, leading to a more open conformation. The increased conformational

478 flexibility enhanced light absorption while depressing fluorescence. This explained

479 why the light absorbance of WSOC increased under basic conditions while the

480 fluorescence intensity increased under acidic conditions. In addition ~~to being influenced~~

481 ~~by conformation, the change in fluorescence spectra of chemical complexes with pH~~

482 ~~can also result from charge transfer from special acidic/basic groups (Phillips and Smith,~~

483 ~~2015; Phillips et al., 2017; Qin et al., 2020). For the results in YC and UR, the~~

484 ~~fluorescence intensity spectra showing turning points at pH2–4 and pH7–10, could be~~

485 ~~related to groups of −COOH and −NH$_2$ and/or −OH, respectively,~~ in Figure 6, the turning

486 point of fluorescence intensity at pH 2–4 and pH 7–10 may be related to acidic/basic

487 groups bound to the fluorophore cores (Cox et al., 1999; Milne et al., 2001; Phillips et

488 al., 2017), and the position variation of the fluorescence peak (λ_{Em}) can further reveal

489 the types of acidic/basic groups (Qin et al., 2022a; Qin et al., 2022c). At XN and LZ,

490 the λ_{Em} redshifted at pH 2–4, indicating the deprotonation of electron-donating groups

491 (e.g., −OH and −NH$_2$), while the λ_{Em} blueshifted at pH 4–7, indicating the deprotonation

492 of electron-withdrawing groups (e.g., −COOH, −C=O, and −NO$_2$). At LZ, the λ_{Em}

493 further redshifted at pH 7–10, suggesting another electron-donating group. In contrast,

at YC and UR, the λ_{Em} redshifted in pH 2–7 and then blueshifted in pH 7–10, suggesting that the deprotonation of electron-donating and electron-withdrawing groups was different from that of LZ.

To identify the potential dominant chemical components of WS-BrC responsible for the pH dependency, we analyzed several fluorescence peaks associated with specific chemical constituents across different pH values (Chen et al., 2003; Fellman et al., 2010). These peaks including peak A (Ex/Em = 225–250/356–440 nm), was classified as humic-like fluorophores (Fu et al., 2015; Qin et al., 2018); peak T (Ex/Em = 270–280/330–355 nm) and peak B (Ex/Em = 270–280/290–310 nm), were classified as protein-like fluorophores (Chen et al., 2003; Birdwell and Engel, 2010); and peak M (Ex/Em = 310–320/380–420 nm), was categorized as oxygenated organic substances (Chen et al., 2003; Qin et al., 2022b). As shown in Figure 7, peak A dominated the variation, contributing 78.5%, 69.1%, 74.1%, and 61.2% of the total variation of all fluorescence peaks in YC, XN, UR, and LZ, respectively. In comparison, other peaks showed moderate variations in the four cities, ranging from 8.3% to 12.4% for peak M, 11.2% to 17.9% for peak T, and 1.6% to 7.6% for peak B. The variation trend of peak A was highly consistent with the trends of the average fluorescence efficiency (AFI/TOC) and the average apparent quantum yield (AQY) over the entire Ex/Em range at each city (Figures 7 and S7). These results suggested that the major fluorophores in all the samples are humic-like compounds. Note that although the dominant contribution comes from the humic-like compound (Peak A) in all the samples, the chemical composition of humic-like compounds among the cities is somewhat different, as indicated by the distinct AQY peak shapes of this peak (Figure S6). These differences can be further elucidated using the PARAFAC model.

3.5. Fluorescent Components

Using the PARAFAC model, we were able to identify six chromophore components

(C1–C6) from EEMs (Figure 8 and Table S2). ~~C1 displays a primary peak (Ex/Em) at 230 nm/375 nm and a secondary peak at 320 nm/375 nm, while C5 exhibits two similar peaks at 210 nm/373 nm and 280 nm/373 nm, albeit with a blue shift. These two chromophores are identified as less oxygenated humic-like substances (LO-HULIS) (Chen et al., 2016; Chen et al., 2021), with different oxidation states between them, and C5 was likely from primary sources such as coal burning and vehicle emissions, while C1 was secondary production.~~ C1 displayed a primary peak (Ex/Em) at 230 nm/375 nm and a secondary peak at 320 nm/375 nm, while C5 exhibited two similar peaks at 210 nm/373 nm and 280 nm/373 nm, albeit with a blueshift. These two chromophores were identified as less oxygenated humic-like substances (LO-HULIS), typically associated with combustion sources (Chen et al., 2016; Chen et al., 2020a; Chen et al., 2021). Therefore, we speculated that C5 is likely a primary chromophore, while a redshift of C1 suggests that C1 is a secondary product (Matos et al., 2015; Wang et al., 2020). C2 exhibited a fluorescence peak at (255 nm/364 nm) and has been observed in previous studies on fossil burning aerosol but has not been defined (Tang et al., 2020; Chen et al., 2020a). C3, peaking at 240 nm/300 nm (Ex) and 414 nm (Em) and was regarded as a highly oxygenated humic-like chromophore (HO-HULIS), commonly considered as a secondary formation (Chen et al., 2016; Yan and Kim, 2017; Cao et al., 2021). Notably, Hawkins et al. (2016) and Aiona et al. (2017) discovered that the fluorescence generated by the aqueous-phase reaction of aldehydes with ammonium sulfate or amines highly matched the HULIS fluorescence peak (Ex < 250/~300 nm, Em > 400 nm) in WSOA of ambient aerosol. C4 (Ex = 225/275 nm and Em = 338 nm) and C6 (Ex = 220 nm, Em = 292 nm) both peaked at a short wavelength and were usually characterized as protein-like fluorophores (PLS) (Yan and Kim, 2017; Wu et al., 2019; Chen et al., 2020a; Chen et al., 2021), but could also be phenol-like substances or other aromatic compounds, especially for urban ambient aerosol samples (Barsotti et al., 2016; Chen et al., 2020a; Cao et al., 2021; Deng et al., 2022). The average relative contributions of chromophores were dominated by HULIS chromophores (C1, C3, and C5) with a total contribution of 56.5–68.4%, followed by PLS chromophores (C4 and C6) (16.5–

22.3%), and then the undefined chromophores (C2) (14.9–20.8%) (Figure 2e). Additionally, significant differences existed in the relative content of each fluorescent component among the four cities. For example, the content of C1 was higher in YC (38.4% vs. 28.7–31.0% in the other three cities) (t-test, $P < 0.01$), the contents of C2 and C4 were higher in LZ (20.8% and 21.1%) than in other three cities (14.7–16.2% and 11.2–18.6%) (t-test, $P < 0.01$), and the content of C3 was significantly higher in UR than in YC, XN and LZ (28.6% vs. 18.8–19.4%) (t-test, $P < 0.01$).

3.6. Source apportionment of WSOA by PMF analysis

Four WSOA factors were identified through PMF analysis on the high-resolution mass spectra of WSOA at four cities, including a water-soluble primary OA (WS-POA), two highly oxidized oxygenated OA (HO-OOA1 and HO-OOA2), and a less oxidized oxygenated OA (LO-OOA) (Figure 9). The mass spectrum of WS-POA was dominated by $C_xH_y^+$ (51%) fragment ions, followed by $C_xH_yO_1^+$ (24%), $C_xH_yO_2^+$ (14%), $C_xH_yN_p^+$ (6%), H_yO_1 (4%), and $C_xH_yO_zN_p^+$ (1%). The WS-POA had the lowest O/C (0.47) and the highest H/C (1.68) among the four factors, but its O/C was much higher than those of online measurement decomposed POA (<0.1) (Xu et al., 2020a; Zhao et al., 2022). In addition to oxygen-containing ions, the WS-POA exhibited a few characteristics similar to those of the online measurement decomposed POA, such as relatively high m/z at 55 and 57 with the m/z 55-to-57 ratio being 2.67, 60 (fraction of signal = 0.39%), and 115 (fraction of signal = 0.21%), which could be related to cooking, biomass burning, and coal combustion, respectively. These results suggested that the WS-POA factor in our study represents mixed primary sources. The mass contribution of WS-POA was 26.2 ± 19.1%, 42.9 ± 15.2%, 30.7 ± 10.2%, and 48.8 ± 9.3% in YC, XN, UR, and LZ, respectively.

The mass spectrum of LO-OOA also displayed a pronounced signal at m/z 115 (signal

fraction = 0.36%), and its concentration was highly correlated with specific PAH signals, such as $C_6H_3^+$, $C_7H_4^+$, $C_8H_5^+$, and $C_9H_5^+$ (Figure 9), indicating that LO-OOA was associated with coal combustion-induced WSOA. However, LO-OOA exhibited significantly higher OS_c (-0.05 vs. -0.74 for LO-OOA and WS-POA, respectively), lower $C_xH_y^+$ ions (33%), and higher combination of oxygenated ions (57% in total), including $C_xH_yO_1^+$ (32%), $C_xH_yO_2^+$ (18%), H_yO_1 (4%), and $C_xH_yO_zN_p^+$ (2%), compared to the primary factor. These implied that LO-OOA likely represented a low oxidation OOA associated with coal combustion-induced WSOA. The same factor was also observed in water-soluble aerosol samples from Beijing during winter (Hu et al., 2020). The mass contribution of LO-OOA was 25.2 ± 15.3%, 10.9 ± 3.3%, 6.4 ± 2.3%, and 7.3 ± 1.6% in YC, XN, UR, and LZ, respectively.

The mass spectrum of HO-OOA1 was characterized by a distinct signal at m/z 44, which accounted for 20.4% of the total signal and was mainly composed of CO_2^+ (94%). Additionally, HO-OOA1 exhibited a high O/C value (0.97), indicating its high oxidation. HO-OOA1 was significantly correlated with nitrate and odd oxygen ($O_x = O_3 + NO_2$), which are the products of photochemical processes (Figure S7), suggesting that HO-OOA1 was photochemically produced (Herndon et al., 2008; Ye et al., 2017). The mass contribution of HO-OOA1 was 29.6 ± 18.1%, 37.2 ± 10.1%, 13.4 ± 10.2%, and 38.3 ± 8.5% in YC, XN, UR, and LZ, respectively. The HO-OOA2 exhibited comparable O/C with that of HO-OOA1 (0.99 vs. 0.97), but it had a higher N/C ratio (0.094 vs. 0.041) and a stronger correlation with RH and sulfate than HO-OOA1, suggesting its potential for aqueous processing production (Sun et al., 2016; Wang et al., 2021). Furthermore, HO-OOA2 exhibited a significant correlation with $CH_2O_2^+$ ($r = 0.48$, P < 0.01), a typical fragment ion for glyoxal, which could be generated from ring-breaking in the aqueous-phase oxidation of polycyclic aromatic hydrocarbons (Chhabra et al., 2010; Wang et al., 2021). The mass contribution of HO-OOA2 were 19.0 ± 5.8%, 8.9 ± 6.2%, 49.5 ± 7.2%, and 5.1 ± 2.7% in YC, XN, UR, and LZ, respectively. Overall, the WSOA in LZ exhibited the highest contribution of POA. Conversely, the WSOA in

609 UR had the highest contribution of HO-OOA2, while the WSOA in YC demonstrated

610 the highest contribution of LO-OOA (Figure 2).

611

612 To further assess the relative light absorption contributions of WSOA from different

613 sources, the four WSOA factors mentioned above were assigned to Abs_{365} using the

614 multiple linear regression model (MLR), as described in the following equation:

615 $Abs_{365} = a \times [WS\text{-}POA] + b \times [LOOA] + c \times [HOOA\text{-}1] + d \times [HOOA\text{-}2]$

616 where [WS-POA], [LOOA], [HOOA-1], and [HOOA-2] are the mass concentrations of

617 WSOA factors; and a, b, c, and d represent regression coefficients (m^2/g), which repre-

618 sents the MAE value for each factor.

619

620 The reconstructed Abs_{365} fits well with the measured Abs_{365}, and the slope is close to 1

621 (Figure S8), indicating the effectiveness of the algorithm. The fitted MAE values were

622 higher for WS-POA and LO-OOA, with values of 1.34 and 1.33 (m^2/g), respectively

623 (Table S4). These values were comparable to those of FF-POA (fossil-fuel POA) (1.35)

624 and LO-OOA (1.24) factors previously determined during the winter in Beijing (Wang

625 et al., 2021). The lower MAE of HO-OOA1 (1.10 m^2/g) was likely attributed to photo-

626 bleaching occurring in photochemical processes (Browne et al., 2019; Chen et al.,

627 2020b; Zhang et al., 2021b). The lowest MAE value for HO-OOA2 (0.58 m^2/g) sug-

628 gested a strong photobleaching effect of the aqueous-phase oxidation process (Wang et

629 al., 2021). The average relative contributions of different WSOA factors to light ab-

630 sorption are shown in Figure 9c. WS-POA was the most important WS-BrC in our study,

631 contributing 60%, 51%, 46%, and 30% of Abs_{365} in LZ, XN, UR, and YC, respectively.

632 HO-OOA1 also played an important role in the absorption of WS-BrC, contributing

633 nearly 30% except in UR (only 13%). HO-OOA2 emerged as a significant contributor

634 to WS-BrC (32%) in UR due to its high-quality contribution (50%), while it was the

635 least contributing factor to Abs_{365} in other three cities (only 2–11%). LO-OOA was an

636 equally important contributor to Abs_{365} as WS-POA in YC (31% vs. 30%), while the

637 contribution was around 10% in other three cities.

638

3.7. Chemical transformations of chromophores

The light-absorption capacity of BrC is closely related to atmospheric aging processes and their chemical composition (Lin et al., 2016; Jiang et al., 2022). To understand the relationship between light-absorption properties and chemical processes, several indexes, including O/C, H/C, N/C, and carbon oxidation state (OSc), were investigated for the relationship with MAE_{365} and AAE (Figure 10). The indexes of O/C and OSc, which reflect the degree of atmospheric aging, were lower in LZ than in other cities (0.58 vs. 0.64–0.77). A significant positive relationship was observed between O/C and MAE_{365} in LZ ($r = 0.57$), while significant negative relationships were observed in YC and UR ($r = -0.70$ and -0.53). These findings suggested that the photo-enhancement phenomenon occurred in LZ, while the photo-bleaching phenomenon took place in the other three cities. Fitting MAE_{365} vs. O/C for all data from the four cities using least-squares linear regression (Figure S9), ~~the fitting trend turns when O/C is about 0.64 ($MAE_{365} = 1.04 \times O/C+0.58$, when O/C<0.64; $MAE_{365} = 1.23 \times O/C+1.90$, when O/C≥0.64)~~ the trend changed around an O/C ratio of 0.64: $MAE_{365} = 1.04 \times O/C + 0.58$ for O/C < 0.64, and $MAE_{365} = -1.23 \times O/C + 1.90$ for O/C ≥ 0.64. A similar phenomenon was found by Jiang et al. (2022) in various polar solvent extracts of $PM_{2.5}$ filters from Beijing, which suggested that chemical processing is dominated by functionalization for the low O/C period, while it is primarily controlled by fragmentation for the high O/C period. Therefore, we inferred that the photo-enhancement phenomenon in LZ is probably due to the initial aging of fresh WSOA.

The variation between MAE_{365} and H/C was broadly opposite to that of O/C. A significant positive correlation between MAE_{365} and H/C was observed in YC and UR, suggesting a higher MAE_{365} for fresh aerosols. MAE_{365} values showed a significantly positive correlation with N/C in YC, XN, and LZ ($r = 0.57$, 0.50, and 0.51, respectively), while a weak correlation in UR ($r = 0.11$), indicating that N-containing organic species

are effectively light-absorbing chromophores (Chen et al., 2018). To elucidate the potential chemical composition and sources of N-containing species, a correlation analysis between MAE_{365} and N-containing fragment ions was conducted. Higher correlation coefficients were found for the $C_xH_yN_p^+$ and $C_xH_yO_zN_p^+$ family ions, such as CHN^+, CH_4N^+, $C_2H_3N^+$, $C_2H_6N^+$, $C_3H_8N^+$, C_2HNO^+, $C_2H_2NO^+$, $C_2H_5NO^+$, and $C_3H_4NO^+$ (Figure S10). These ions may be associated with amine, imine, N-heterocyclic compounds (e.g., imidazole), organonitrates, and nitroaromatic compounds, which have been proven to be important BrC components in ambient aerosol (Farmer et al., 2010; Sun et al., 2012; Kim et al., 2019; Kasthuriarachchi et al., 2020; Ditto et al., 2022; Jiang et al., 2022).

The relationship between AAE and O/C was also investigated. In YC, AAE increased significantly with rising O/C (slope = 2.62, r = 0.55), which could be attributed to the significant chemical oxidation and the formation of O-containing functional groups with weakly light-absorbing characteristics of WSOA (Sumlin et al., 2017; Zeng et al., 2021), resulting in a shift in the absorption spectrum towards UV wavelengths (Zhang et al., 2013; Mo et al., 2018). Nevertheless, a significant negative relationship between AAE and O/C was observed in LZ (slope = −1.41, r = −0.51). The initial oxidation occurring in LZ introduced functional groups to form auxochrome or chromophores, leading to absorption enhancement and an absorption spectrum red-shift (Lin et al., 2015; Zeng et al., 2021; Jiang et al., 2022). Additionally, the AAE values showed a roughly decreasing trend with increasing N/C in the four cities, possibly due to the abundance of N-heteroatoms leading to a red shift in the absorption spectrum (Jiang et al., 2022).

Crossing-correlation among fluorescent chromophores and chemical components of $PM_{2.5}$ were performed to infer the possible sources and atmospheric chemical processes of WS-BrC (Figure 11a). The results revealed that C1, C3, and C6 were tightly

correlated with SNA, particularly sulfate, indicating contributions from secondary production sources. In contrast, C2, C4, and C5 exhibited tight correlations with primary species like EC, K^+, and Cl^-, suggesting origins from primary emission sources. Furthermore, the fluorescent chromophores were assigned to different WSOA factors based on ~~their correlation.~~ Pearson's correlation analysis between the relative abundance of the four PMF factors and the relative content of the six PARAFAC components. For example, C2, C4, and C5, identified as primary chromophore components, significantly correlated with WS-POA. C1, characterized as less oxygenated humic-like components, significantly correlated with LO-OOA, representing secondary chromophoric components with less oxidation. C3, identified as highly oxygenated humic-like components, strongly correlated with HO-OOA2. Notably, there was a significant positive correlation between C3 and HO-OOA1 when excluding UR data (Figure S11). Thus C3 was likely to represent secondary chromophoric components with a high degree of oxidation, formed through either aqueous-phase or photochemical oxidation, with different contributions from these two aging pathways in different cities of our study. C6 exhibited a significant correlation with HO-OOA2, and the EEM spectra of C6 overlapped highly with phenol chromophore (Barsotti et al., 2016; Chen et al., 2020a), implying that C6 might be a phenol-like chromophore and an aqueous-phase oxidation product. Recent studies have indicated the presence of benzene and its derivatives in atmospheric waters such as clouds and fog (Raja et al., 2009). Benzene reacts readily with hydroxyl radicals in the aqueous phase ($k_{OH} = 4.7 \times 10^5$ μM^{-1} min^{-1}), which is much faster than its reaction to other atmospheric radicals such as ozone ($k_{O_3} = 6.1 \times 10^{-6}$ μM^{-1} min^{-1}) and nitrate radicals ($k_{NO_3} = 4.0 \times 10^{-1}$ μM^{-1} min^{-1}) or photolysis in the gas phase (Minakata et al., 2009). Thus, the atmospheric chemistry reaction of benzenes is likely initiated by •OH in the aqueous-phase, leading to the formation of phenol-like chromophores (Borrás and Tortajada-Genaro, 2012; Heath et al., 2013; Faust et al., 2017).

By combining the information provided above into a Van Krevelen plot (H:C vs. O:C),

commonly used to illustrate the evolution of organic aerosols (Heald et al., 2010; Ng et al., 2011; Canagaratna et al., 2015), a tight relationship between the evolution of chemical processes and the light absorbance of chromophores was clearly revealed. Note that in the Van Krevelen plot, each WSOA factor is colored by its fitted MAE_{365}, with the size of each WSOA factor representing the average contribution to Abs_{365}, and the PARAFAC components are also assigned to distinct WSOA factors based on their relevance to each factor. Overall, the aging processes from fresh species (WS-POA) to LO-OOA and HO-OOAs, along the direction of increasing OSc, were clearly associated with a photobleaching phenomenon, as evidenced by a decrease/increase in MAE365/AAE values. The slope from WS-POA to each OOA component could be used to some extent to describe this photobleaching phenomenon, i.e., –0.91 for WS-POA & LO-OOA, –0.53 for WS-POA & HO-OOA1, and –0.34 for WS-POA & HO-OOA2. A lower slope (closer to –1) could be related to the addition of carboxylic acid functional groups, while higher slopes (such as –0.5) could be related to the addition of alcohol/peroxide functional groups. Additionally, the slopes for each dataset from the four cities exhibited variation: –1.01 at LZ, –0.89 at XN, –0.78 at UR, and –0.71 at YC. This variation further underscores the different chemical processes and optical properties in each city.

Figure 11c displays the EEM profiles of the six PARAFAC components (indicated by dashed line) along with their fluorescence peak positions (Ex/Em) (represented by circles C1–C6), as well as their corresponding compound categories. The potential origins and atmospheric chemical transformations of these chromophores are further revealed by correlating the PMF results. The classification of the highly oxygenated and less oxygenated species regions proposed by Chen et al. (2016) closely matches with our research findings. However, our results are divided into three distinct categories: fresh species, less oxidized species, and highly oxidized species, with each region circled by a different shade of brown box in Figure 11c. Note that the chemical transformation of

the loss of primary chromophores (fresh species) and the generation of secondary chromophores (less oxidized and highly oxidized species) can occur through either photochemical oxidation or aqueous-phase oxidation, with different contributions from the two aging pathways in different cities. Additionally, certain chromophores formed from high oxidation processes exhibit short emission wavelengths, which were originally classified as PLS chromophores, providing a reference for determining PLS sources and processes in future studies.

4. Conclusions

In this study, a comprehensive comparison was conducted regarding the optical properties, potential sources, and chemical processes of WSOA using atmospheric aerosols collected from four typical cities, namely Yinchuan (YC), Xining (XN), Urumqi (UR), and Lanzhou (LZ). The main conclusions and environmental implications are obtained as follows.

Firstly, the optical properties of WSOA were found to be influenced by its chemical composition. The MAE_{365}, HIX, and BIX values of XN (1.24 m^2/g, 1.29, 1.49) and LZ (1.19 m^2/g, 1.16, 1.52) were higher, lower, and higher than those of YC (1.07 m^2/g, 1.32, 1.48) and UR (0.78 m^2/g, 1.85, 1.28), possibly due to a higher contribution of fresh WSOA in XN and LZ and a greater degree of humification and aging/oxidation of WSOA in YC and UR. Secondly, the optical properties of WSOA were found to be influenced by pH variation. The integrated absorbance (300–450 nm) and MAE_{365} exhibited a monotonically increasing trend with rising pH in four cities. The impact of pH on EEM spectra was much more complex, involving the rigidity and planarity of molecule structure and the protonation/deprotonation of electron-withdrawing groups (–COOH and $-NO_2$) and electron-donating groups (–NH_2 and –OH) connected to the fluorophore nuclei. The WSOA in YC and LZ were found to be most sensitive to pH variation and exhibited distinct trends, indicating that their chemical structures are rich

781 in different types of acid/base functional groups. Thirdly, changes in the optical prop-
782 erties of WSOA were observed during aging/oxidation processes. Obvious photo-
783 bleaching was observed in YC and UR, while photo-enhancement was observed in LZ,
784 reflecting the role of the initial aging (functionalization) and further oxidation (frag-
785 mentation) of fresh WSOA on the optical properties of WS-BrC based on the analysis
786 of optical properties and bulk chemical characteristics. Finally, the analysis combining
787 chromophores with WSOA factors can be used to illustrate the chemical processes and
788 optical variation by V-K plot and EEM plot, which is useful for understanding the dom-
789 inant chemical pathway at each city.

790

791 Overall, this study provides insights into the optical properties, sources, and chemical
792 transformations of WS-BrC. These insights will provide an important reference for fu-
793 ture studies to determine the sources and processes of atmospheric chromophores and
794 further help to estimate the climatic effects of atmospheric aerosols and control carbo-
795 naceous aerosol pollution.

796

797 **Data availability**
798 The data used in this study can be accessed on request from corresponding author.

799

800 **Author contributions**
801 JX designed the research and MZ, HW, LG and WL collected samples. MZ processed
802 data, plotted the figures, and wrote the manuscript when JX and XZ gave constructive
803 discussion. LZ and WZ had an active role in supporting the experimental work. All
804 authors contributed to the discussions of the results and refinement of the manuscript.

805

806 **Competing interests**
807 The authors declare that they have no conflict of interests.

808

809 **Acknowledgment**

This work was partially supported by the National Natural Science Foundation of China (41977189) and the Key Laboratory of Cryospheric Sciences Scientific Research Foundation (SKLCS-ZZ-2023).

References

Aiona, P. K., Lee, H. J., Leslie, R., Lin, P., Laskin, A., Laskin, J., and Nizkorodov, S. A.: Photochemistry of Products of the Aqueous Reaction of Methylglyoxal with Ammonium Sulfate, ACS Earth Sp. Chem., 1, 522-532, https://doi.org/10.1021/acsearthspacechem.7b00075, 2017.

Andreae, M. O. and Gelencsér, A.: Black carbon or brown carbon? The nature of light-absorbing carbonaceous aerosols, Atmos. Chem. Phys., 6, 3131-3148, https://doi.org/10.5194/acp-6-3131-2006, 2006.

Barsotti, F., Ghigo, G., and Vione, D.: Computational assessment of the fluorescence emission of phenol oligomers: A possible insight into the fluorescence properties of humic-like substances (HULIS), J. Photochem. Photobiol. A Chem., 315, 87-93, https://doi.org/10.1016/j.jphotochem.2015.09.012, 2016.

Baylon, P., Jaffe, D. A., Hall, S. R., Ullmann, K., Alvarado, M. J., and Lefer, B. L.: Impact of Biomass Burning Plumes on Photolysis Rates and Ozone Formation at the Mount Bachelor Observatory, J. Geophys. Res.-Atmos., 123, 2272-2284, https://doi.org/10.1002/2017jd027341, 2018.

Bikkina, S. and Sarin, M.: Brown carbon in the continental outflow to the North Indian Ocean, Environ. Sci.-Proc. Imp., 21, 970-987, https://doi.org/110.1039/c9em00089e, 2019.

Birdwell, J. E. and Engel, A. S.: Characterization of dissolved organic matter in cave and spring waters using UV–Vis absorbance and fluorescence spectroscopy, Org. Geochem., 41, 270-280, https://doi.org/10.1016/j.orggeochem.2009.11.002, 2010.

Borrás, E. and Tortajada-Genaro, L. A.: Secondary organic aerosol formation from the photo-oxidation of benzene, Atmos. Environ., 47, 154-163, https://doi.org/10.1016/j.atmosenv.2011.11.020, 2012.

Browne, E. C., Zhang, X., Franklin, J. P., Ridley, K. J., Kirchstetter, T. W., Wilson, K. R., Cappa, C. D., and Kroll, J. H.: Effect of heterogeneous oxidative aging on light absorption by biomass burning organic aerosol, Aerosol Sci. Technol., 53, 663-674, https://doi.org/10.1080/02786826.2019.1599321, 2019.

Cai, J., Zeng, X., Zhi, G., Gligorovski, S., Sheng, G., Yu, Z., Wang, X., and Peng, P. a.: Molecular composition and photochemical evolution of water-soluble organic carbon (WSOC) extracted from field biomass burning aerosols using high-resolution mass spectrometry, Atmos. Chem. Phys., 20, 6115-6128, https://doi.org/10.5194/acp-20-6115-2020, 2020.

Canagaratna, M. R., Jimenez, J. L., Kroll, J. H., Chen, Q., Kessler, S. H., Massoli, P., Hildebrandt Ruiz, L., Fortner, E., Williams, L. R., Wilson, K. R., Surratt, J. D., Donahue, N. M., Jayne, J. T., and Worsnop, D. R.: Elemental ratio measurements of organic compounds using aerosol mass spectrometry: characterization, improved calibration, and implications, Atmos. Chem. Phys., 15, 253-272, https://doi.org/10.5194/acp-15-253-2015, 2015.

Cao, T., Li, M., Zou, C., Fan, X., Song, J., Jia, W., Yu, C., Yu, Z., and Peng, P. a.: Chemical

composition, optical properties, and oxidative potential of water- and methanol-soluble organic compounds emitted from the combustion of biomass materials and coal, Atmos. Chem. Phys., 21, 13187-13205, https://doi.org/10.5194/acp-21-13187-2021, 2021.

Chen, Q., Hua, X., Li, J., Chang, T., and Wang, Y.: Diurnal evolutions and sources of water-soluble chromophoric aerosols over Xi'an during haze event, in Northwest China, Sci. Total Environ., 786, 147412, https://doi.org/10.1016/j.scitotenv.2021.147412, 2021.

Chen, Q., Li, J., Hua, X., Jiang, X., Mu, Z., Wang, M., Wang, J., Shan, M., Yang, X., Fan, X., Song, J., Wang, Y., Guan, D., and Du, L.: Identification of species and sources of atmospheric chromophores by fluorescence excitation-emission matrix with parallel factor analysis, Sci. Total Environ., 718, 137322, https://doi.org/10.1016/j.scitotenv.2020.137322, 2020a.

Chen, Q., Miyazaki, Y., Kawamura, K., Matsumoto, K., Coburn, S., Volkamer, R., Iwamoto, Y., Kagami, S., Deng, Y., Ogawa, S., Ramasamy, S., Kato, S., Ida, A., Kajii, Y., and Mochida, M.: Characterization of Chromophoric Water-Soluble Organic Matter in Urban, Forest, and Marine Aerosols by HR-ToF-AMS Analysis and Excitation-Emission Matrix Spectroscopy, Environ. Sci. Technol., 50, 10351-10360, https://doi.org/10.1021/acs.est.6b01643, 2016.

Chen, W., Westerhoff, P., Leenheer, J. A., and Booksh, K.: Fluorescence excitation-emission matrix regional integration to quantify spectra for dissolved organic matter, Environ. Sci. Technol., 37, 5701-5710, https://doi.org/10.1021/es034354c, 2003.

Chen, Y. and Bond, T. C.: Light absorption by organic carbon from wood combustion, Atmos. Chem. Phys., 10, 1773-1787, https://doi.org/10.5194/acp-10-1773-2010, 2010.

Chen, Y., Ge, X., Chen, H., Xie, X., Chen, Y., Wang, J., Ye, Z., Bao, M., Zhang, Y., and Chen, M.: Seasonal light absorption properties of water-soluble brown carbon in atmospheric fine particles in Nanjing, China, Atmos. Environ., 187, 230-240, https://doi.org/10.1016/j.atmosenv.2018.06.002, 2018.

Chen, Y., Xie, X., Shi, Z., Li, Y., Gai, X., Wang, J., Li, H., Wu, Y., Zhao, X., Chen, M., and Ge, X.: Brown carbon in atmospheric fine particles in Yangzhou, China: Light absorption properties and source apportionment, Atmos. Res., 244, 105028, https://doi.org/10.1016/j.atmosres.2020.105028, 2020b.

Cheng, Y., He, K. B., Engling, G., Weber, R., Liu, J. M., Du, Z. Y., and Dong, S. P.: Brown and black carbon in Beijing aerosol: Implications for the effects of brown coating on light absorption by black carbon, Sci. Total Environ., 599-600, 1047-1055, https://doi.org/10.1016/j.scitotenv.2017.05.061, 2017.

Cheng, Y., He, K.-b., Du, Z.-y., Engling, G., Liu, J.-m., Ma, Y.-l., Zheng, M., and Weber, R. J.: The characteristics of brown carbon aerosol during winter in Beijing, Atmos. Environ., 127, 355-364, https://doi.org/10.1016/j.atmosenv.2015.12.035, 2016.

Chhabra, P. S., Flagan, R. C., and Seinfeld, J. H.: Elemental analysis of chamber organic aerosol using an aerodyne high-resolution aerosol mass spectrometer, Atmos. Chem. Phys., 10, 4111-4131, https://doi.org/10.5194/acp-10-4111-2010, 2010.

Choudhary, V., Gupta, T., and Zhao, R.: Evolution of Brown Carbon Aerosols during Atmospheric Long-Range Transport in the South Asian Outflow and Himalayan Cryosphere, ACS Earth Sp. Chem., 6, 2335-2347, https://doi.org/10.1021/acsearthspacechem.2c00047, 2022.

Choudhary, V., Rajput, P., and Gupta, T.: Absorption properties and forcing efficiency of light-absorbing water-soluble organic aerosols: Seasonal and spatial variability, Environ. Pollut., 272,

895   115932, https://doi.org/10.1016/j.envpol.2020.115932, 2021.

896   Chow, J. C., Watson, J. G., Chen, L. W., Chang, M. C., Robinson, N. F., Trimble, D., and Kohl,

897   S.: The IMPROVE_A temperature protocol for thermal/optical carbon analysis: maintaining

898   consistency with a long-term database, J. Air Waste Manag. Assoc., 57, 1014-1023,

899   https://doi.org/10.3155/1047-3289.57.9.1014, 2007.

900   Cox, J. S., Smith, D. S., Warren, L. A., and Ferris, F. G.: Characterizing Heterogeneous

901   Bacterial Surface Functional Groups Using Discrete Affinity Spectra for Proton Binding,

902   Environ. Sci. Technol., 33, 4514-4521, https://doi.org/10.1021/es990627l, 1999.

903   Dao, X., Di, S., Zhang, X., Gao, P., Wang, L., Yan, L., Tang, G., He, L., Krafft, T., and Zhang,

904   F.: Composition and sources of particulate matter in the Beijing-Tianjin-Hebei region and its

905   surrounding   areas   during   the   heating   season,   Chemosphere,   291,   132779,

906   https://doi.org/10.1016/j.chemosphere.2021.132779, 2022.

907   Deng, J., Ma, H., Wang, X., Zhong, S., Zhang, Z., Zhu, J., Fan, Y., Hu, W., Wu, L., Li, X., Ren,

908   L., Pavuluri, C. M., Pan, X., Sun, Y., Wang, Z., Kawamura, K., and Fu, P.: Measurement report:

909   Optical properties and sources of water-soluble brown carbon in Tianjin, North China – insights

910   from   organic   molecular   compositions,   Atmos.   Chem.   Phys.,   22,   6449-6470,

911   https://doi.org/10.5194/acp-22-6449-2022, 2022.

912   Ditto, J. C., Machesky, J., and Gentner, D. R.: Analysis of reduced and oxidized nitrogen-

913   containing organic compounds at a coastal site in summer and winter, Atmos. Chem. Phys., 22,

914   3045-3065, https://doi.org/10.5194/acp-22-3045-2022, 2022.

915   Du, Z., He, K., Cheng, Y., Duan, F., Ma, Y., Liu, J., Zhang, X., Zheng, M., and Weber, R.: A

916   yearlong study of water-soluble organic carbon in Beijing II: Light absorption properties,

917   Atmos. Environ., 89, 235-241, https://doi.org/10.1016/j.atmosenv.2014.02.022, 2014.

918   Fan, X., Cao, T., Yu, X., Wang, Y., Xiao, X., Li, F., Xie, Y., Ji, W., Song, J., and Peng, P. a.: The

919   evolutionary behavior of chromophoric brown carbon during ozone aging of fine particles from

920   biomass burning, Atmos. Chem. Phys., 20, 4593-4605, https://doi.org/10.5194/acp-20-4593-

921   2020, 2020.

922   Fan, X. J., Wei, S. Y., Zhu, M. B., Song, J. Z., and Peng, P. A.: Comprehensive characterization

923   of humic-like substances in smoke PM2.5 emitted from the combustion of biomass materials

924   and fossil fuels, Atmos. Chem. Phys., 16, 13321-13340, https://doi.org/10.5194/acp-16-13321-

925   2016, 2016.

926   Fan, X. J., Cao, T., Yu, X. F., Song, J. Z., Wang, Y., Xiao, X., Xie, Y., and Li, F. Y.: Emission

927   characteristics and optical properties of extractable brown carbon from residential wood

928   combustion, China Environ. Sci., 39, 3215-3224, https://doi.org/10.19674/j.cnki.issn1000-

929   6923.2019.0380, 2019.

930   Farmer, D. K., Matsunaga, A., Docherty, K. S., Surratt, J. D., Seinfeld, J. H., Ziemann, P. J.,

931   and Jimenez, J. L.: Response of an aerosol mass spectrometer to organonitrates and

932   organosulfates and implications for atmospheric chemistry, Proc. Natl. Acad. Sci. U. S. A., 107,

933   6670-6675, https://doi.org/10.1073/pnas.0912340107, 2010.

934   Faust, J. A., Wong, J. P., Lee, A. K., and Abbatt, J. P.: Role of Aerosol Liquid Water in Secondary

935   Organic Aerosol Formation from Volatile Organic Compounds, Environ. Sci. Technol., 51,

936   1405-1413, https://doi.org/10.1021/acs.est.6b04700, 2017.

937   Fellman, J. B., Hood, E., and Spencer, R. G. M.: Fluorescence spectroscopy opens new

938   windows into dissolved organic matter dynamics in freshwater ecosystems: A review, Limnol.

939   Oceanogr., 55, 2452-2462, https://doi.org/10.4319/lo.2010.55.6.2452, 2010.

940   Fu, P., Kawamura, K., Chen, J., Qin, M., Ren, L., Sun, Y., Wang, Z., Barrie, L. A., Tachibana,
941   E., Ding, A., and Yamashita, Y.: Fluorescent water-soluble organic aerosols in the High Arctic
942   atmosphere, Sci. Rep., 5, 9845, https://doi.org/10.1038/srep09845, 2015.

943   Ge, X., Li, L., Chen, Y., Chen, H., Wu, D., Wang, J., Xie, X., Ge, S., Ye, Z., Xu, J., and Chen,
944   M.: Aerosol characteristics and sources in Yangzhou, China resolved by offline aerosol mass
945   spectrometry and other techniques, Environ. Pollut., 225, 74-85,
946   https://doi.org/10.1016/j.envpol.2017.03.044, 2017.

947   Ghosh, K. and Schnitzer, M.: Fluorescence Excitation-Spectra and Viscosity Behavior of a
948   Fulvic-Acid and Its Copper and Iron Complexes, Soil Sci. Soc. Am. J., 45, 25-29,
949   https://doi.org/10.2136/sssaj1981.03615995004500010005x, 1981.

950   Hawkins, L. N., Lemire, A. N., Galloway, M. M., Corrigan, A. L., Turley, J. J., Espelien, B. M.,
951   and De Haan, D. O.: Maillard Chemistry in Clouds and Aqueous Aerosol As a Source of
952   Atmospheric Humic-Like Substances, Environ. Sci. Technol., 50, 7443-7452,
953   https://doi.org/10.1021/acs.est.6b00909, 2016.

954   Heald, C. L., Kroll, J. H., Jimenez, J. L., Docherty, K. S., DeCarlo, P. F., Aiken, A. C., Chen,
955   Q., Martin, S. T., Farmer, D. K., and Artaxo, P.: A simplified description of the evolution of
956   organic aerosol composition in the atmosphere, Geophys. Res. Lett., 37, L08803,
957   https://doi.org/10.1029/2010gl042737, 2010.

958   Heath, A. A., Ehrenhauser, F. S., and Valsaraj, K. T.: Effects of temperature, oxygen level, ionic
959   strength, and pH on the reaction of benzene with hydroxyl radicals in aqueous atmospheric
960   systems, J. Environ. Chem. Eng., 1, 822-830, https://doi.org/10.1016/j.jece.2013.07.023, 2013.

961   Hecobian, A., Zhang, X., Zheng, M., Frank, N., Edgerton, E. S., and Weber, R. J.: Water-Soluble
962   Organic Aerosol material and the light-absorption characteristics of aqueous extracts measured
963   over the Southeastern United States, Atmos. Chem. Phys., 10, 5965-5977,
964   https://doi.org/10.5194/acp-10-5965-2010, 2010.

965   Herndon, S. C., Onasch, T. B., Wood, E. C., Kroll, J. H., Canagaratna, M. R., Jayne, J. T., Zavala,
966   M. A., Knighton, W. B., Mazzoleni, C., Dubey, M. K., Ulbrich, I. M., Jimenez, J. L., Seila, R.,
967   de Gouw, J. A., de Foy, B., Fast, J., Molina, L. T., Kolb, C. E., and Worsnop, D. R.: Correlation
968   of secondary organic aerosol with odd oxygen in Mexico City, Geophys. Res. Lett., 35, L15804,
969   https://doi.org/10.1029/2008gl034058, 2008.

970   Hu, R., Xu, Q., Wang, S., Hua, Y., Bhattarai, N., Jiang, J., Song, Y., Daellenbach, K. R., Qi, L.,
971   Prevot, A. S. H., and Hao, J.: Chemical characteristics and sources of water-soluble organic
972   aerosol in southwest suburb of Beijing, J. Environ. Sci., 95, 99-110,
973   https://doi.org/10.1016/j.jes.2020.04.004, 2020.

974   Huang, R. J., Yang, L., Cao, J., Chen, Y., Chen, Q., Li, Y., Duan, J., Zhu, C., Dai, W., Wang, K.,
975   Lin, C., Ni, H., Corbin, J. C., Wu, Y., Zhang, R., Tie, X., Hoffmann, T., O'Dowd, C., and Dusek,
976   U.: Brown Carbon Aerosol in Urban Xi'an, Northwest China: The Composition and Light
977   Absorption Properties, Environ. Sci. Technol., 52, 6825-6833,
978   https://doi.org/10.1021/acs.est.8b02386, 2018.

979   Huang, R. J., Yang, L., Shen, J., Yuan, W., Gong, Y., Guo, J., Cao, W., Duan, J., Ni, H., Zhu, C.,
980   Dai, W., Li, Y., Chen, Y., Chen, Q., Wu, Y., Zhang, R., Dusek, U., O'Dowd, C., and Hoffmann,
981   T.: Water-Insoluble Organics Dominate Brown Carbon in Wintertime Urban Aerosol of China:
982   Chemical Characteristics and Optical Properties, Environ. Sci. Technol., 54, 7836-7847,

983 https://doi.org/10.1021/acs.est.0c01149, 2020.

984 Huang, R. J., Zhang, Y., Bozzetti, C., Ho, K. F., Cao, J. J., Han, Y., Daellenbach, K. R., Slowik,
985 J. G., Platt, S. M., Canonaco, F., Zotter, P., Wolf, R., Pieber, S. M., Bruns, E. A., Crippa, M.,
986 Ciarelli, G., Piazzalunga, A., Schwikowski, M., Abbaszade, G., Schnelle-Kreis, J.,
987 Zimmermann, R., An, Z., Szidat, S., Baltensperger, U., El Haddad, I., and Prevot, A. S.: High
988 secondary aerosol contribution to particulate pollution during haze events in China, Nature, 514,
989 218-222, https://doi.org/10.1038/nature13774, 2014.

990 Jiang, X., Liu, D., Li, Q., Tian, P., Wu, Y., Li, S., Hu, K., Ding, S., Bi, K., Li, R., Huang, M.,
991 Ding, D., Chen, Q., Kong, S., Li, W., Pang, Y., and He, D.: Connecting the Light Absorption of
992 Atmospheric Organic Aerosols with Oxidation State and Polarity, Environ. Sci. Technol., 56,
993 12873-12885, https://doi.org/10.1021/acs.est.2c02202, 2022.

994 Kasthuriarachchi, N. Y., Rivellini, L. H., Chen, X., Li, Y. J., and Lee, A. K. Y.: Effect of Relative
995 Humidity on Secondary Brown Carbon Formation in Aqueous Droplets, Environ. Sci. Technol.,
996 54, 13207-13216, https://doi.org/10.1021/acs.est.0c01239, 2020.

997 Kim, H., Collier, S., Ge, X., Xu, J., Sun, Y., Jiang, W., Wang, Y., Herckes, P., and Zhang, Q.:
998 Chemical processing of water-soluble species and formation of secondary organic aerosol in
999 fogs, Atmos. Environ., 200, 158-166, https://doi.org/10.1016/j.atmosenv.2018.11.062, 2019.

1000 Kuwata, M., Zorn, S. R., and Martin, S. T.: Using elemental ratios to predict the density of
1001 organic material composed of carbon, hydrogen, and oxygen, Environ. Sci. Technol., 46, 787-
1002 794, https://doi.org/10.1021/es202525q, 2012.

1003 Lambe, A. T., Cappa, C. D., Massoli, P., Onasch, T. B., Forestieri, S. D., Martin, A. T.,
1004 Cummings, M. J., Croasdale, D. R., Brune, W. H., Worsnop, D. R., and Davidovits, P.:
1005 Relationship between oxidation level and optical properties of secondary organic aerosol,
1006 Environ. Sci. Technol., 47, 6349-6357, https://doi.org/10.1021/es401043j, 2013.

1007 Laskin, A., Laskin, J., and Nizkorodov, S. A.: Chemistry of atmospheric brown carbon, Chem.
1008 Rev., 115, 4335-4382, https://doi.org/10.1021/cr5006167, 2015.

1009 Lawaetz, A. J. and Stedmon, C. A.: Fluorescence intensity calibration using the Raman scatter
1010 peak of water, Appl. Spectrosc., 63, 936-940, https://doi.org/10.1366/000370209788964548,
1011 2009.

1012 Lee, H. J., Laskin, A., Laskin, J., and Nizkorodov, S. A.: Excitation-emission spectra and
1013 fluorescence quantum yields for fresh and aged biogenic secondary organic aerosols, Environ.
1014 Sci. Technol., 47, 5763-5770, https://doi.org/10.1021/es400644c, 2013.

1015 Lei, L., Zhou, W., Chen, C., He, Y., Li, Z., Sun, J., Tang, X., Fu, P., Wang, Z., and Sun, Y.:
1016 Long-term characterization of aerosol chemistry in cold season from 2013 to 2020 in Beijing,
1017 China, Environ. Pollut., 268, 115952, https://doi.org/10.1016/j.envpol.2020.115952, 2021.

1018 Lei, Y., Shen, Z., Zhang, T., Zhang, Q., Wang, Q., Sun, J., Gong, X., Cao, J., Xu, H., Liu, S.,
1019 and Yang, L.: Optical source profiles of brown carbon in size-resolved particulate matter from
1020 typical domestic biofuel burning over Guanzhong Plain, China, Sci. Total Environ., 622-623,
1021 244-251, https://doi.org/10.1016/j.scitotenv.2017.11.353, 2018.

1022 Li, C., He, Q., Hettiyadura, A. P. S., Kafer, U., Shmul, G., Meidan, D., Zimmermann, R., Brown,
1023 S. S., George, C., Laskin, A., and Rudich, Y.: Formation of Secondary Brown Carbon in
1024 Biomass Burning Aerosol Proxies through NO3 Radical Reactions, Environ. Sci. Technol., 54,
1025 1395-1405, https://doi.org/10.1021/acs.est.9b05641, 2020a.

1026 Li, H., Qin, X., Wang, G., Xu, J., Wang, L., Lu, D., Liu, C., Zheng, H., Liu, J., Huang, K., and

Deng, C.: Conjoint impacts of continental outflows and marine sources on brown carbon in the East China sea: Abundances, optical properties, and formation processes, Atmos. Environ., 273, https://doi.org/10.1016/j.atmosenv.2022.118959, 2022.

Li, J., Zhang, Q., Wang, G., Li, J., Wu, C., Liu, L., Wang, J., Jiang, W., Li, L., Ho, K. F., and Cao, J.: Optical properties and molecular compositions of water-soluble and water-insoluble brown carbon (BrC) aerosols in northwest China, Atmos. Chem. Phys., 20, 4889-4904, https://doi.org/10.5194/acp-20-4889-2020, 2020b.

Lin, P., Bluvshtein, N., Rudich, Y., Nizkorodov, S. A., Laskin, J., and Laskin, A.: Molecular Chemistry of Atmospheric Brown Carbon Inferred from a Nationwide Biomass Burning Event, Environ. Sci. Technol., 51, 11561-11570, https://doi.org/10.1021/acs.est.7b02276, 2017.

Lin, P., Liu, J., Shilling, J. E., Kathmann, S. M., Laskin, J., and Laskin, A.: Molecular characterization of brown carbon (BrC) chromophores in secondary organic aerosol generated from photo-oxidation of toluene, Phys. Chem. Chem. Phys., 17, 23312-23325, https://doi.org/10.1039/c5cp02563j, 2015.

Lin, P., Aiona, P. K., Li, Y., Shiraiwa, M., Laskin, J., Nizkorodov, S. A., and Laskin, A.: Molecular Characterization of Brown Carbon in Biomass Burning Aerosol Particles, Environ. Sci. Technol., 50, 11815-11824, https://doi.org/10.1021/acs.est.6b03024, 2016.

Liu, C., Liu, Y., Chen, T., Liu, J., and He, H.: Rate constant and secondary organic aerosol formation from the gas-phase reaction of eugenol with hydroxyl radicals, Atmos. Chem. Phys., 19, 2001-2013, https://doi.org/10.5194/acp-19-2001-2019, 2019.

Liu, J., Bergin, M., Guo, H., King, L., Kotra, N., Edgerton, E., and Weber, R. J.: Size-resolved measurements of brown carbon in water and methanol extracts and estimates of their contribution to ambient fine-particle light absorption, Atmos. Chem. Phys., 13, 12389-12404, https://doi.org/10.5194/acp-13-12389-2013, 2013.

Liu, J. M., Wang, P. F., Zhang, H. L., Du, Z. Y., Zheng, B., Yu, Q. Q., Zheng, G. J., Ma, Y. L., Zheng, M., Cheng, Y., Zhang, Q., and He, K. B.: Integration of field observation and air quality modeling to characterize Beijing aerosol in different seasons, Chemosphere, 242, 125195, https://doi.org/10.1016/j.chemosphere.2019.125195, 2020.

Matos, J. T. V., Freire, S. M. S. C., Duarte, R. M. B. O., and Duarte, A. C.: Natural organic matter in urban aerosols: Comparison between water and alkaline soluble components using excitation–emission matrix fluorescence spectroscopy and multiway data analysis, Atmos. Environ., 102, 1-10, https://doi.org/10.1016/j.atmosenv.2014.11.042, 2015.

McKnight, D. M., Boyer, E. W., Westerhoff, P. K., Doran, P. T., Kulbe, T., and Andersen, D. T.: Spectrofluorometric characterization of dissolved organic matter for indication of precursor organic material and aromaticity, Limnol. Oceanogr., 46, 38-48, https://doi.org/10.4319/lo.2001.46.1.0038, 2001.

Mei, Y., Wang, L., and Wu, F.: Effects of water chemistry and concentrations of dissolved organic matter on its fluorescence characteristics and molecular conformation, Chin. J. Geochem., 28, 413-420, https://doi.org/10.1007/s11631-009-0413-2, 2009.

Milne, C. J., Kinniburgh, D. G., and Tipping, E.: Generic NICA-Donnan model parameters for proton binding by humic substances, Environ. Sci. Technol., 35, 2049-2059, https://doi.org/10.1021/es000123j, 2001.

Minakata, D., Li, K., Westerhoff, P., and Crittenden, J.: Development of a group contribution method to predict aqueous phase hydroxyl radical (HO*) reaction rate constants, Environ. Sci.

1071   Technol., 43, 6220-6227, https://doi.org/10.1021/es900956c, 2009.

1072   Mo, Y., Li, J., Jiang, B., Su, T., Geng, X., Liu, J., Jiang, H., Shen, C., Ding, P., Zhong, G., Cheng,
1073   Z., Liao, Y., Tian, C., Chen, Y., and Zhang, G.: Sources, compositions, and optical properties of
1074   humic-like substances in Beijing during the 2014 APEC summit: Results from dual carbon
1075   isotope and Fourier-transform ion cyclotron resonance mass spectrometry analyses, Environ.
1076   Pollut., 239, 322-331, https://doi.org/10.1016/j.envpol.2018.04.041, 2018.

1077   Moise, T., Flores, J. M., and Rudich, Y.: Optical properties of secondary organic aerosols and
1078   their changes by chemical processes, Chem. Rev., 115, 4400-4439,
1079   https://doi.org/10.1021/cr5005259, 2015.

1080   Mok, J., Krotkov, N. A., Arola, A., Torres, O., Jethva, H., Andrade, M., Labow, G., Eck, T. F.,
1081   Li, Z., Dickerson, R. R., Stenchikov, G. L., Osipov, S., and Ren, X.: Impacts of brown carbon
1082   from biomass burning on surface UV and ozone photochemistry in the Amazon Basin, Sci. Rep.,
1083   6, 36940, https://doi.org/10.1038/srep36940, 2016.

1084   Murphy, K. R., Stedmon, C. A., Graeber, D., and Bro, R.: Fluorescence spectroscopy and multi-
1085   way techniques. PARAFAC, Anal. Methods,, 5, 6557-6566,
1086   https://doi.org/10.1039/c3ay41160e, 2013.

1087   Ng, N. L., Canagaratna, M. R., Jimenez, J. L., Chhabra, P. S., Seinfeld, J. H., and Worsnop, D.
1088   R.: Changes in organic aerosol composition with aging inferred from aerosol mass spectra,
1089   Atmos. Chem. Phys., 11, 6465-6474, https://doi.org/10.5194/acp-11-6465-2011, 2011.

1090   Ni, H., Huang, R. J., Pieber, S. M., Corbin, J. C., Stefenelli, G., Pospisilova, V., Klein, F., Gysel-
1091   Beer, M., Yang, L., Baltensperger, U., Haddad, I. E., Slowik, J. G., Cao, J., Prevot, A. S. H.,
1092   and Dusek, U.: Brown Carbon in Primary and Aged Coal Combustion Emission, Environ. Sci.
1093   Technol., 55, 5701-5710, https://doi.org/10.1021/acs.est.0c08084, 2021.

1094   Ohno, T.: Fluorescence inner-filtering correction for determining the humification index of
1095   dissolved organic matter, Environ. Sci. Technol., 742-746, https://doi.org/10.1021/es0155276,
1096   2002.

1097   Phillips, S. M. and Smith, G. D.: Further evidence for charge transfer complexes in brown
1098   carbon aerosols from excitation-emission matrix fluorescence spectroscopy, J. Phys. Chem. A,
1099   119, 4545-4551, https://doi.org/10.1021/jp510709e, 2015.

1100   Phillips, S. M., Bellcross, A. D., and Smith, G. D.: Light Absorption by Brown Carbon in the
1101   Southeastern United States is pH-dependent, Environ. Sci. Technol., 51, 6782-6790,
1102   https://doi.org/10.1021/acs.est.7b01116, 2017.

1103   Psichoudaki, M. and Pandis, S. N.: Atmospheric aerosol water-soluble organic carbon
1104   measurement: a theoretical analysis, Environ. Sci. Technol., 47, 9791-9798,
1105   https://doi.org/10.1021/es402270y, 2013.

1106   Qin, J., Zhang, L., Qin, Y., Shi, S., Li, J., Gao, Y., Tan, J., and Wang, X.: pH-Dependent
1107   Chemical Transformations of Humic-Like Substances and Further Cognitions Revealed by
1108   Optical Methods, Environ. Sci. Technol., 56, 7578-7587,
1109   https://doi.org/10.1021/acs.est.1c07729, 2022a.

1110   Qin, J., Zhang, L., Zhou, X., Duan, J., Mu, S., Xiao, K., Hu, J., and Tan, J.: Fluorescence
1111   fingerprinting properties for exploring water-soluble organic compounds in PM2.5 in an
1112   industrial city of northwest China, Atmos. Environ., 184, 203-211,
1113   https://doi.org/10.1016/j.atmosenv.2018.04.049, 2018.

1114   Qin, J., Tan, J., Zhou, X., Yang, Y., Qin, Y., Wang, X., Shi, S., Xiao, K., and Wang, X.:

Measurement report: Particle-size-dependent fluorescence properties of water-soluble organic compounds (WSOCs) and their atmospheric implications for the aging of WSOCs, Atmos. Chem. Phys., 22, 465-479, https://doi.org/10.5194/acp-22-465-2022, 2022b.

Qin, Y., Yang, Y., Qin, J., Zhang, L., Guo, S., Zhou, X., Chen, R., Tan, J., Xiao, K., and Wang, X.: pH-Responsive Fluorescence EEM to Titrate the Interaction between Fluorophores and Acid/Base Groups in Water-Soluble Organic Compounds of PM2.5, Environ. Sci. Technol. Lett., 8, 108-113, https://doi.org/10.1021/acs.estlett.0c00645, 2020.

Qin, Y., Qin, J., Wang, X., Xiao, K., Qi, T., Gao, Y., Zhou, X., Shi, S., Li, J., Gao, J., Zhang, Z., Tan, J., Zhang, Y., and Chen, R.: Measurement report: Investigation of pH- and particle-size-dependent chemical and optical properties of water-soluble organic carbon: implications for its sources and aging processes, Atmos. Chem. Phys., 22, 13845-13859, https://doi.org/10.5194/acp-22-13845-2022, 2022c.

Raja, S., Raghunathan, R., Kommalapati, R. R., Shen, X., Collett, J. L., and Valsaraj, K. T.: Organic composition of fogwater in the Texas–Louisiana gulf coast corridor, Atmos. Environ., 43, 4214-4222, https://doi.org/10.1016/j.atmosenv.2009.05.029, 2009.

Saleh, R.: From Measurements to Models: Toward Accurate Representation of Brown Carbon in Climate Calculations, Curr. Pollut. Rep., 6, 90-104, https://doi.org/10.1007/s40726-020-00139-3, 2020.

Shamjad, P. M., Tripathi, S. N., Thamban, N. M., and Vreeland, H.: Refractive Index and Absorption Attribution of Highly Absorbing Brown Carbon Aerosols from an Urban Indian City-Kanpur, Sci. Rep., 6, 37735, https://doi.org/10.1038/srep37735, 2016.

Shan, Y., Guan, D., Hubacek, K., Zheng, B., Davis, S. J., Jia, L., Liu, J., Liu, Z., Fromer, N., Mi, Z., Meng, J., Deng, X., Li, Y., Lin, J., Schroeder, H., Weisz, H., and Schellnhuber, H. J.: City-level climate change mitigation in China, Sci. Adv., 4, eaaq0390, https://doi.org/10.1126/sciadv.aaq0390, 2018.

Song, C., Gyawali, M., Zaveri, R. A., Shilling, J. E., and Arnott, W. P.: Light absorption by secondary organic aerosol fromα-pinene: Effects of oxidants, seed aerosol acidity, and relative humidity, J. Geophys. Res.-Atmos., 118, 11741–711749, https://doi.org/10.1002/jgrd.50767, 2013.

Sumlin, B. J., Pandey, A., Walker, M. J., Pattison, R. S., Williams, B. J., and Chakrabarty, R. K.: Atmospheric Photooxidation Diminishes Light Absorption by Primary Brown Carbon Aerosol from Biomass Burning, Environ. Sci. Technol. Lett., 4, 540-545, https://doi.org/10.1021/acs.estlett.7b00393, 2017.

Sun, W., Huo, J., Li, R., Wang, D., Yao, L., Fu, Q., and Feng, J.: Effects of energy structure differences on chemical compositions and respiratory health of PM2.5 during late autumn and winter in China, Sci. Total Environ., 824, 153850, https://doi.org/10.1016/j.scitotenv.2022.153850, 2022.

Sun, Y., Wang, Z., Fu, P., Jiang, Q., Yang, T., Li, J., and Ge, X.: The impact of relative humidity on aerosol composition and evolution processes during wintertime in Beijing, China, Atmos. Environ., 77, 927-934, https://doi.org/10.1016/j.atmosenv.2013.06.019, 2013.

Sun, Y. L., Zhang, Q., Schwab, J. J., Yang, T., Ng, N. L., and Demerjian, K. L.: Factor analysis of combined organic and inorganic aerosol mass spectra from high resolution aerosol mass spectrometer measurements, Atmos. Chem. Phys., 12, 8537-8551, https://doi.org/10.5194/acp-12-8537-2012, 2012.

Sun, Y. L., Du, W., Fu, P. Q., Wang, Q. Q., Li, J., Ge, X. L., Zhang, Q., Zhu, C. M., Ren, L. J., Xu, W. Q., Zhao, J., Han, T. T., Worsnop, D. R., and Wang, Z. F.: Primary and secondary aerosols in Beijing in winter: sources, variations and processes, Atmos. Chem. Phys., 16, 8309-8329, https://doi.org/10.5194/acp-16-8309-2016, 2016.

Sun, Y. L., He, Y., Kuang, Y., Xu, W. Y., Song, S. J., Ma, N., Tao, J. C., Cheng, P., Wu, C., Su, H., Cheng, Y. F., Xie, C. H., Chen, C., Lei, L., Qiu, Y. M., Fu, P. Q., Croteau, P., and Worsnop, D. R.: Chemical Differences Between PM1 and PM2.5 in Highly Polluted Environment and Implications in Air Pollution Studies, Geophys. Res. Lett., 47, e2019GL086288, https://doi.org/10.1029/2019GL086288, 2020.

Tan, J., Xiang, P., Zhou, X., Duan, J., Ma, Y., He, K., Cheng, Y., Yu, J., and Querol, X.: Chemical characterization of humic-like substances (HULIS) in PM2.5 in Lanzhou, China, Sci. Total Environ., 573, 1481-1490, https://doi.org/10.1016/j.scitotenv.2016.08.025, 2016.

Tang, J., Li, J., Su, T., Han, Y., Mo, Y., Jiang, H., Cui, M., Jiang, B., Chen, Y., Tang, J., Song, J., Peng, P. a., and Zhang, G.: Molecular compositions and optical properties of dissolved brown carbon in biomass burning, coal combustion, and vehicle emission aerosols illuminated by excitation–emission matrix spectroscopy and Fourier transform ion cyclotron resonance mass spectrometry analysis, Atmos. Chem. Phys., 20, 2513-2532, https://doi.org/10.5194/acp-20-2513-2020, 2020.

Vidovic, K., Kroflic, A., Sala, M., and Grgic, I.: Aqueous-Phase Brown Carbon Formation from Aromatic Precursors under Sunlight Conditions, Atmosphere, 11, 131, https://doi.org/10.3390/atmos11020131, 2020.

Vidovic, K., Lasic Jurkovic, D., Sala, M., Kroflic, A., and Grgic, I.: Nighttime Aqueous-Phase Formation of Nitrocatechols in the Atmospheric Condensed Phase, Environ. Sci. Technol., 52, 9722-9730, https://doi.org/10.1021/acs.est.8b01161, 2018.

Wang, H., Zhang, L., Huo, T., Wang, B., Yang, F., Chen, Y., Tian, M., Qiao, B., and Peng, C.: Application of parallel factor analysis model to decompose excitation-emission matrix fluorescence spectra for characterizing sources of water-soluble brown carbon in PM2.5, Atmos. Environ., 223, https://doi.org/10.1016/j.atmosenv.2019.117192, 2020.

Wang, J., Ye, J., Zhang, Q., Zhao, J., Wu, Y., Li, J., Liu, D., Li, W., Zhang, Y., Wu, C., Xie, C., Qin, Y., Lei, Y., Huang, X., Guo, J., Liu, P., Fu, P., Li, Y., Lee, H. C., Choi, H., Zhang, J., Liao, H., Chen, M., Sun, Y., Ge, X., Martin, S. T., and Jacob, D. J.: Aqueous production of secondary organic aerosol from fossil-fuel emissions in winter Beijing haze, Proc. Natl. Acad. Sci. U. S. A., 118, e2022179118, https://doi.org/10.1073/pnas.2022179118, 2021.

Wang, X., Heald, C. L., Liu, J., Weber, R. J., Campuzano-Jost, P., Jimenez, J. L., Schwarz, J. P., and Perring, A. E.: Exploring the observational constraints on the simulation of brown carbon, Atmos. Chem. Phys., 18, 635-653, https://doi.org/10.5194/acp-18-635-2018, 2018.

Wang, Y., Hu, M., Lin, P., Tan, T., Li, M., Xu, N., Zheng, J., Du, Z., Qin, Y., Wu, Y., Lu, S., Song, Y., Wu, Z., Guo, S., Zeng, L., Huang, X., and He, L.: Enhancement in Particulate Organic Nitrogen and Light Absorption of Humic-Like Substances over Tibetan Plateau Due to Long-Range Transported Biomass Burning Emissions, Environ. Sci. Technol., 53, 14222-14232, https://doi.org/10.1021/acs.est.9b06152, 2019.

Washenfelder, R. A., Attwood, A. R., Brock, C. A., Guo, H., Xu, L., Weber, R. J., Ng, N. L., Allen, H. M., Ayres, B. R., Baumann, K., Cohen, R. C., Draper, D. C., Duffey, K. C., Edgerton, E., Fry, J. L., Hu, W. W., Jimenez, J. L., Palm, B. B., Romer, P., Stone, E. A., Wooldridge, P. J.,

and Brown, S. S.: Biomass burning dominates brown carbon absorption in the rural southeastern United States, Geophys. Res. Lett., 42, 653-664, https://doi.org/10.1002/2014gl062444, 2015.

Wen, H., Zhou, Y., Xu, X., Wang, T., Chen, Q., Chen, Q., Li, W., Wang, Z., Huang, Z., Zhou, T., Shi, J., Bi, J., Ji, M., and Wang, X.: Water-soluble brown carbon in atmospheric aerosols along the transport pathway of Asian dust: Optical properties, chemical compositions, and potential sources, Sci. Total Environ., 789, 147971, https://doi.org/10.1016/j.scitotenv.2021.147971, 2021.

Wu, G., Ram, K., Fu, P., Wang, W., Zhang, Y., Liu, X., Stone, E. A., Pradhan, B. B., Dangol, P. M., Panday, A. K., Wan, X., Bai, Z., Kang, S., Zhang, Q., and Cong, Z.: Water-Soluble Brown Carbon in Atmospheric Aerosols from Godavari (Nepal), a Regional Representative of South Asia, Environ. Sci. Technol., 53, 3471-3479, https://doi.org/10.1021/acs.est.9b00596, 2019.

Xu, J., Ge, X., Zhang, X., Zhao, W., Zhang, R., and Zhang, Y.: COVID-19 Impact on the Concentration and Composition of Submicron Particulate Matter in a Typical City of Northwest China, Geophys. Res. Lett., 47, e2020GL089035, https://doi.org/10.1029/2020GL089035, 2020a.

Xu, J., Hettiyadura, A. P. S., Liu, Y., Zhang, X., Kang, S., and Laskin, A.: Regional Differences of Chemical Composition and Optical Properties of Aerosols in the Tibetan Plateau, J. Geophys. Res.-Atmos., 125, e2019JD031226, https://doi.org/10.1029/2019jd031226, 2020b.

Xu, J., Hettiyadura, A. P. S., Liu, Y., Zhang, X., Kang, S., and Laskin, A.: Atmospheric Brown Carbon on the Tibetan Plateau: Regional Differences in Chemical Composition and Light Absorption Properties, Environ. Sci. Technol. Lett., 9, 219-225, https://doi.org/10.1021/acs.estlett.2c00016, 2022.

Xu, J., Zhang, Q., Chen, M., Ge, X., Ren, J., and Qin, D.: Chemical composition, sources, and processes of urban aerosols during summertime in northwest China: insights from high-resolution aerosol mass spectrometry, Atmos. Chem. Phys., 14, 12593-12611, https://doi.org/10.5194/acp-14-12593-2014, 2014.

Xu, J., Zhang, Q., Li, X., Ge, X., Xiao, C., Ren, J., and Qin, D.: Dissolved organic matter and inorganic ions in a central Himalayan glacier--insights into chemical composition and atmospheric sources, Environ. Sci. Technol., 47, 6181-6188,, https://doi.org/10.1021/es4009882, 2013.

Xu, J., Shi, J., Zhang, Q., Ge, X., Canonaco, F., Prévôt, A. S. H., Vonwiller, M., Szidat, S., Ge, J., Ma, J., An, Y., Kang, S., and Qin, D.: Wintertime organic and inorganic aerosols in Lanzhou, China: sources, processes, and comparison with the results during summer, Atmos. Chem. Phys., 16, 14937-14957, https://doi.org/10.5194/acp-16-14937-2016, 2016.

Xu, J. Z., Zhang, Q., Wang, Z. B., Yu, G. M., Ge, X. L., and Qin, X.: Chemical composition and size distribution of summertime PM2.5 at a high altitude remote location in the northeast of the Qinghai–Xizang (Tibet) Plateau: insights into aerosol sources and processing in free troposphere, Atmos. Chem. Phys., 15, 5069-5081, https://doi.org/10.5194/acp-15-5069-2015, 2015.

Yan, G. and Kim, G.: Speciation and Sources of Brown Carbon in Precipitation at Seoul, Korea: Insights from Excitation-Emission Matrix Spectroscopy and Carbon Isotopic Analysis, Environ. Sci. Technol., 51, 11580-11587, https://doi.org/10.1021/acs.est.7b02892, 2017.

Yang, H., Xu, G., Mao, H., and Wang, Y.: Spatiotemporal Variation in Precipitation and Water

Vapor Transport Over Central Asia in Winter and Summer Under Global Warming, Front. Earth Sci., 8, 297, https://doi.org/10.3389/feart.2020.00297, 2020a.

Yang, Y., Qin, J., Qi, T., Zhou, X., Chen, R., Tan, J., Xiao, K., Ji, D., He, K., and Chen, X.: Fluorescence characteristics of particulate water-soluble organic compounds emitted from coal-fired boilers, Atmos. Environ., 223, https://doi.org/10.1016/j.atmosenv.2020.117297, 2020b.

Ye, Z., Liu, J., Gu, A., Feng, F., Liu, Y., Bi, C., Xu, J., Li, L., Chen, H., Chen, Y., Dai, L., Zhou, Q., and Ge, X.: Chemical characterization of fine particulate matter in Changzhou, China, and source apportionment with offline aerosol mass spectrometry, Atmos. Chem. Phys., 17, 2573-2592, https://doi.org/10.5194/acp-17-2573-2017, 2017.

Yuan, W., Huang, R.-J., Yang, L., Ni, H., Wang, T., Cao, W., Duan, J., Guo, J., Huang, H., and Hoffmann, T.: Concentrations, optical properties and sources of humic-like substances (HULIS) in fine particulate matter in Xi'an, Northwest China, Sci. Total Environ., 789, https://doi.org/10.1016/j.scitotenv.2021.147902, 2021.

Yue, S., Ren, L., Song, T., Li, L., Xie, Q., Li, W., Kang, M., Zhao, W., Wei, L., Ren, H., Sun, Y., Wang, Z., Ellam, R. M., Liu, C. Q., Kawamura, K., and Fu, P.: Abundance and Diurnal Trends of Fluorescent Bioaerosols in the Troposphere over Mt. Tai, China, in Spring, J. Geophys. Res.-Atmos., 124, 4158-4173, https://doi.org/10.1029/2018jd029486, 2019.

Zeng, L., Zhang, A., Wang, Y., Wagner, N. L., Katich, J. M., Schwarz, J. P., Schill, G. P., Brock, C., Froyd, K. D., Murphy, D. M., Williamson, C. J., Kupc, A., Scheuer, E., Dibb, J., and Weber, R. J.: Global Measurements of Brown Carbon and Estimated Direct Radiative Effects, Geophys. Res. Lett., 47, e2020GL088747, https://doi.org/10.1029/2020GL088747, 2020.

Zeng, Y. L., Ning, Y. L., Shen, Z. X., Zhang, L. M., Zhang, T., Lei, Y. L., Zhang, Q., Li, G. H., Xu, H. M., Ho, S. S. H., and Cao, J. J.: The Roles of N, S, and O in Molecular Absorption Features of Brown Carbon in PM2.5 in a Typical Semi-Arid Megacity in Northwestern China, J. Geophys. Res.-Atmos., 126, e2021JD034791, https://doi.org/10.1029/2021JD034791, 2021.

Zhang, Q., Shen, Z., Zhang, L., Zeng, Y., Ning, Z., Zhang, T., Lei, Y., Wang, Q., Li, G., Sun, J., Westerdahl, D., Xu, H., and Cao, J.: Investigation of Primary and Secondary Particulate Brown Carbon in Two Chinese Cities of Xi'an and Hong Kong in Wintertime, Environ. Sci. Technol., 54, 3803-3813, https://doi.org/10.1021/acs.est.9b05332, 2020.

Zhang, X., Lin, Y. H., Surratt, J. D., and Weber, R. J.: Sources, composition and absorption Angstrom exponent of light-absorbing organic components in aerosol extracts from the Los Angeles Basin, Environ. Sci. Technol., 47, 3685-3693, https://doi.org/10.1021/es305047b, 2013.

Zhang, X., Ding, X., Talifu, D., Wang, X., Abulizi, A., Maihemuti, M., and Rekefu, S.: Humidity and PM2.5 composition determine atmospheric light extinction in the arid region of northwest China, J. Environ. Sci., 100, 279-286, https://doi.org/10.1016/j.jes.2020.07.007, 2021a.

Zhang, X., Xu, J., Kang, S., Sun, J., Shi, J., Gong, C., Sun, X., Du, H., Ge, X., and Zhang, Q.: Regional Differences in the Light Absorption Properties of Fine Particulate Matter Over the Tibetan Plateau: Insights From HR-ToF-AMS and Aethalometer Measurements, J. Geophys. Res.-Atmos., 126, e2021JD035562, https://doi.org/10.1029/2021jd035562, 2021b.

Zhang, Y.-L., El-Haddad, I., Huang, R.-J., Ho, K.-F., Cao, J.-J., Han, Y., Zotter, P., Bozzetti, C., Daellenbach, K. R., Slowik, J. G., Salazar, G., Prévôt, A. S. H., and Szidat, S.: Large contribution of fossil fuel derived secondary organic carbon to water soluble organic aerosols

in winter haze in China, Atmos. Chem. Phys., 18, 4005-4017, https://doi.org/10.5194/acp-18-4005-2018, 2018.

Zhang, Y., Xu, J., Shi, J., Xie, C., Ge, X., Wang, J., Kang, S., and Zhang, Q.: Light absorption by water-soluble organic carbon in atmospheric fine particles in the central Tibetan Plateau, Environ. Sci. Pollut. Res. Int., 24, 21386-21397, https://doi.org/10.1007/s11356-017-9688-8, 2017.

Zhang, Y., Shi, Z., Wang, Y., Liu, L., Zhang, J., Li, J., Xia, Y., Ding, X., Liu, D., Kong, S., Niu, H., Fu, P., Zhang, X., and Li, W.: Fine particles from village air in northern China in winter: Large contribution of primary organic aerosols from residential solid fuel burning, Environ. Pollut., 272, 116420, https://doi.org/10.1016/j.envpol.2020.116420, 2021c.

Zhao, R., Lee, A. K. Y., Huang, L., Li, X., Yang, F., and Abbatt, J. P. D.: Photochemical processing of aqueous atmospheric brown carbon, Atmos. Chem. Phys., 15, 6087-6100, https://doi.org/10.5194/acp-15-6087-2015, 2015.

Zhao, W., Zhang, X., Zhai, L., Shen, X., and Xu, J.: Chemical characterization and sources of submicron aerosols in Lhasa on the Qinghai–Tibet Plateau: Insights from high-resolution mass spectrometry, Sci. Total Environ., 815, 152866, https://doi.org/10.1016/j.scitotenv.2021.152866, 2022.

Zhou, Y., West, C. P., Hettiyadura, A. P. S., Niu, X., Wen, H., Cui, J., Shi, T., Pu, W., Wang, X., and Laskin, A.: Measurement report: Molecular composition, optical properties, and radiative effects of water-soluble organic carbon in snowpack samples from northern Xinjiang, China, Atmos. Chem. Phys., 21, 8531-8555, https://doi.org/10.5194/acp-21-8531-2021, 2021.

Zhou, Y., West, C. P., Hettiyadura, A. P. S., Pu, W., Shi, T., Niu, X., Wen, H., Cui, J., Wang, X., and Laskin, A.: Molecular Characterization of Water-Soluble Brown Carbon Chromophores in Snowpack from Northern Xinjiang, China, Environ. Sci. Technol., 56, 4173-4186, https://doi.org/10.1021/acs.est.1c07972, 2022.

Zhu, C. S., Cao, J. J., Huang, R. J., Shen, Z. X., Wang, Q. Y., and Zhang, N. N.: Light absorption properties of brown carbon over the southeastern Tibetan Plateau, Sci. Total Environ., 625, 246-251, https://doi.org/10.1016/j.scitotenv.2017.12.183, 2018.

Zou, C., Cao, T., Li, M., Song, J., Jiang, B., Jia, W., Li, J., Ding, X., Yu, Z., Zhang, G., and Peng, P. a.: Measurement report: Changes in light absorption and molecular composition of water-soluble humic-like substances during a winter haze bloom-decay process in Guangzhou, China, Atmos. Chem. Phys., 23, 963-979, https://doi.org/10.5194/acp-23-963-2023, 2023.

Zsolnay, A., Baigar, E., Jimenez, M., Steinweg, B., and Saccomandi, F.: Differentiating with fluorescence spectroscopy the sources of dissolved organic matter in soils subjected to drying, 45-50, https://doi.org/10.1016/s0045-6535(98)00166-0, 1999, 1999.

1326 **Figures**
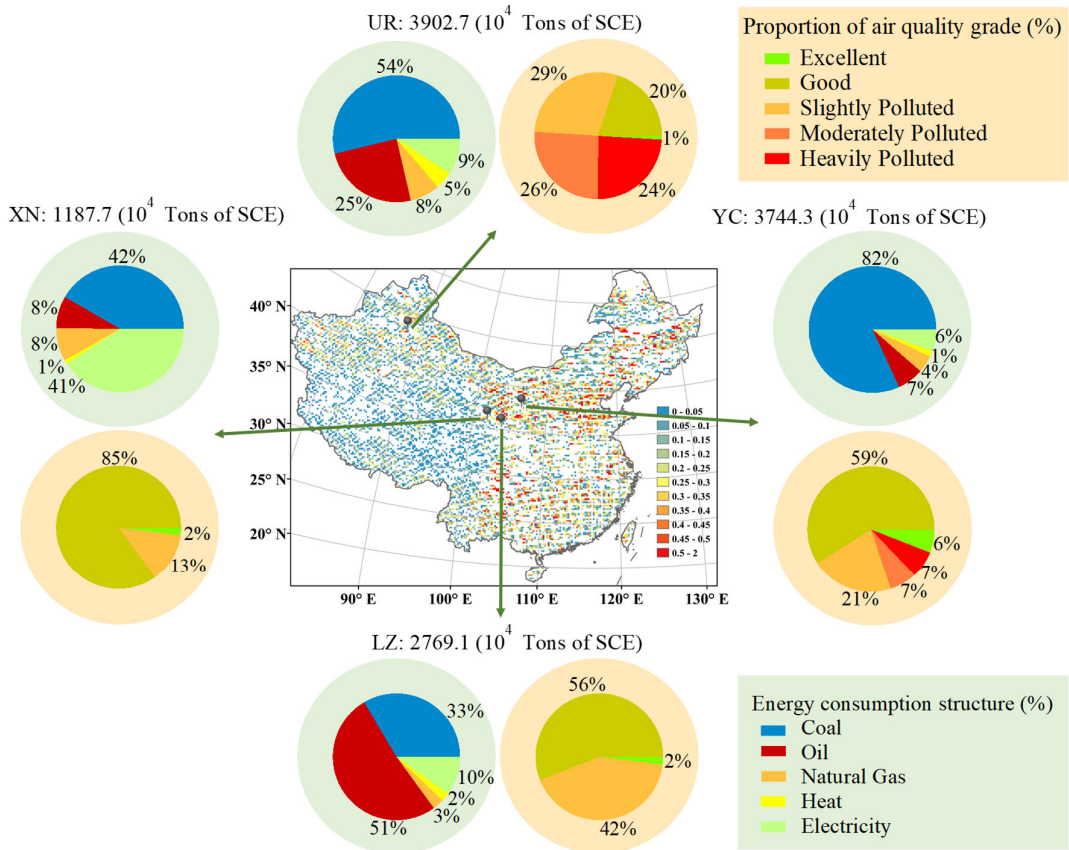
1327
1328 Figure 1. Location map for the sampling sites in this study, and the corresponding energy structure
1329 in each city and air quality in each city during 2019. The locations of the four cities is also shown
1330 the spatial variation of SO_2 concentration in China (resolution of 0.25°*0.25°), retrieved from OMI
1331 satellite data over the whole sampling period of 2019/12-2020/1 (http://www.satdatafresh.com/).
1332 Pie charts around the map show the energy consumption structure of industrial enterprises above
1333 the designated size during 2019 (source: China Energy Statistical Yearbook) and the proportion of
1334 urban air quality grades during the sampling period at YC, XN, UR, and LZ
1335 (https://www.zq12369.com/), respectively.
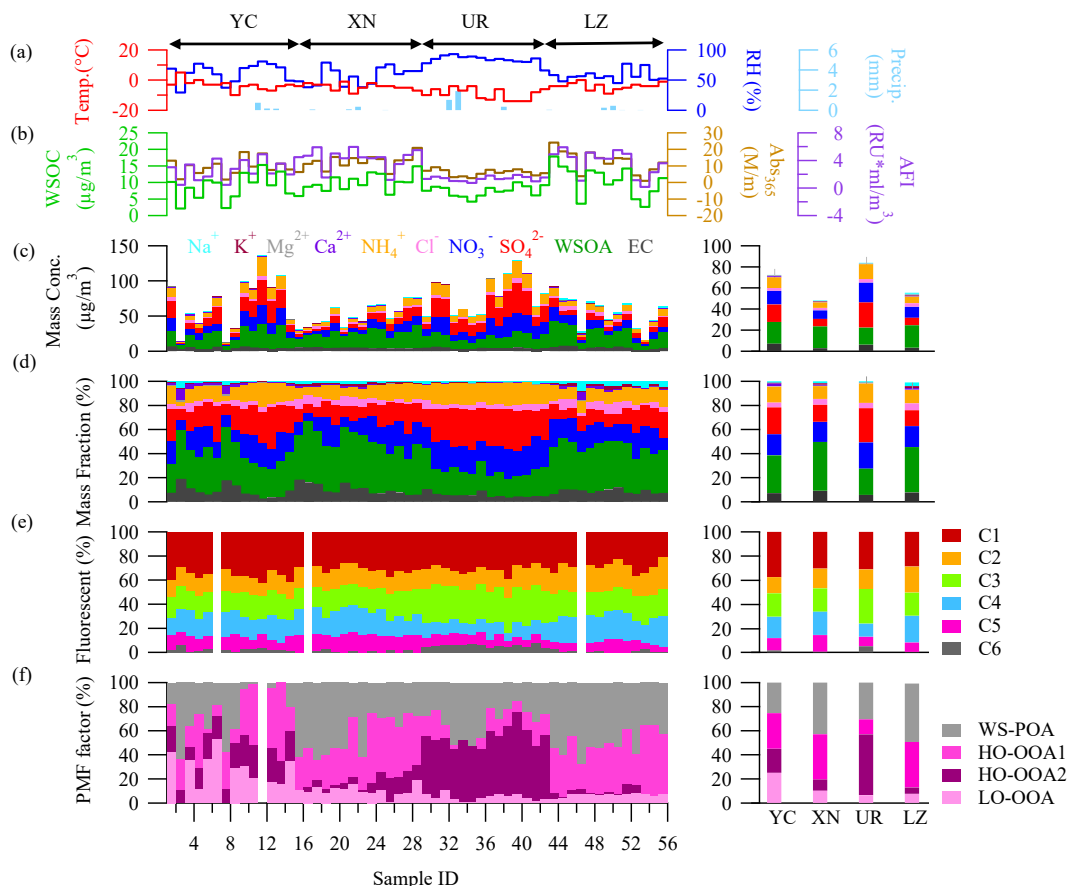
1336

1337 Figure 2. The combo plot for the results of aerosol samples versus sample IDs in this study. (a)

1338 Meteorological condition during the sampling including air temperature, relative humidity, and pre-

1339 cipitation; (b) WSOC concentrations, the light-absorption (Abs), and average fluorescence intensity

1340 (AFI) of WSOA; (c) the concentrations of total identified species (~~WSIs~~WSIIs, OM, and EC); (d)

1341 The relative abundance of total identified species; (e) The relative abundances of the identified six

1342 fluorescent components by PARAFAC analysis; (f) Mass contributions of the factors resolved by

1343 PMF analysis on WSOA.

1344
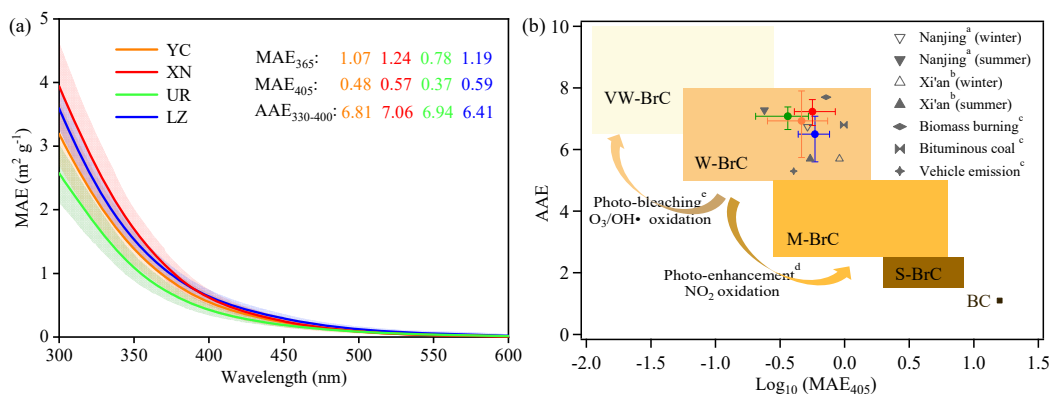
1345

1346 Figure 3. (a) The average MAE spectrum and their standard deviations of WS-BrC in each city

1347 represented by different colors. (b) Graphical representation of the optical-based BrC classes in the

log₁₀(MAE₄₀₅)-AAE space (Saleh, 2020). The shaded areas respectively indicate very weakly (VW), weakly (W), moderately (M), and strongly (S) absorbing BrC and absorbing BC. Grey marks indicate the data from previous studies about ambient BrC aerosol, i.e., [a]Chen et al. (2018) [b](Huang et al., 2018) [c](Tang et al., 2020). The curve with the arrowhead displays the variation tendency of optical properties of the lab-generated BrC aerosol and aged in the presence of NO_3 or O_3/OH radicals, i.e., [d](Li et al., 2020a) [e](Browne et al., 2019).
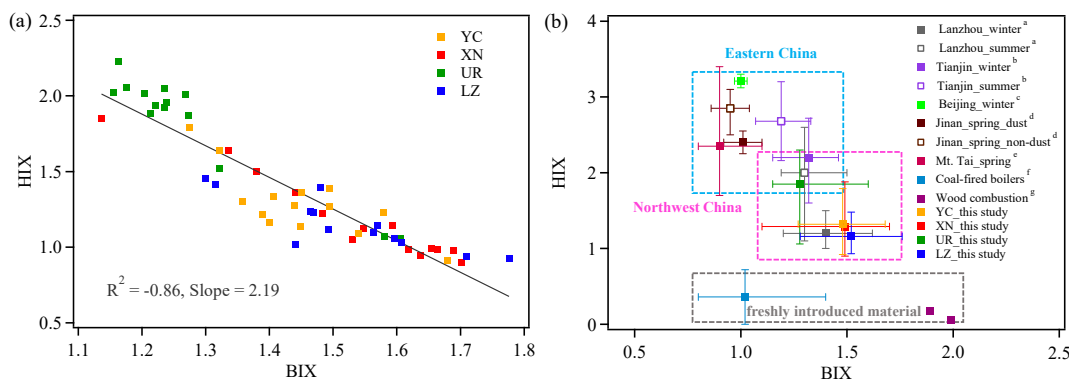
Figure 4. (a) Scatter plots of the humification index (HIX) as a function of the biological index (BIX) for WSOA in four cities. (b) Comparison plot of HIX versus BIX for this study and previous literatures, including WSOA from ambient aerosols in Lanzhou [a](Qin et al., 2018), Tianjin [b](Deng et al., 2022), Beijing [c](Qin et al., 2022b), Jinan [d](Wen et al., 2021), Mt. Tai [e](Yue et al., 2019), and from coal-fired aerosols [f](Yang et al., 2020b), and biomass burning aerosols [g](Fan et al., 2019).
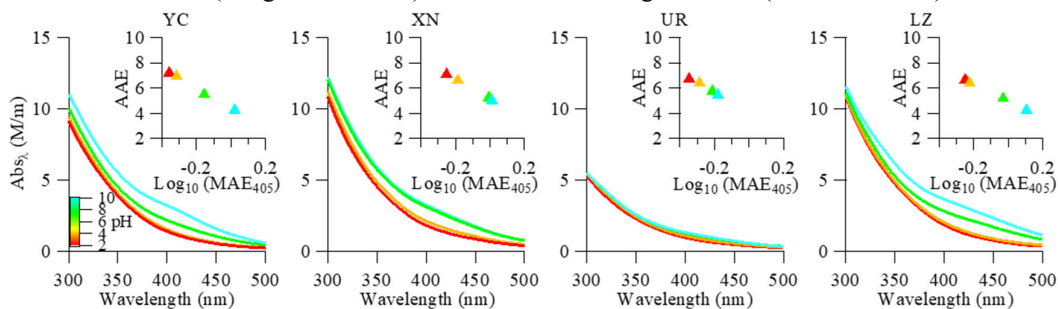
Figure 5. The Influence of pH on absorbance spectra (the insert figure shows the log₁₀(MAE₄₀₅)-AAE values at different pH).
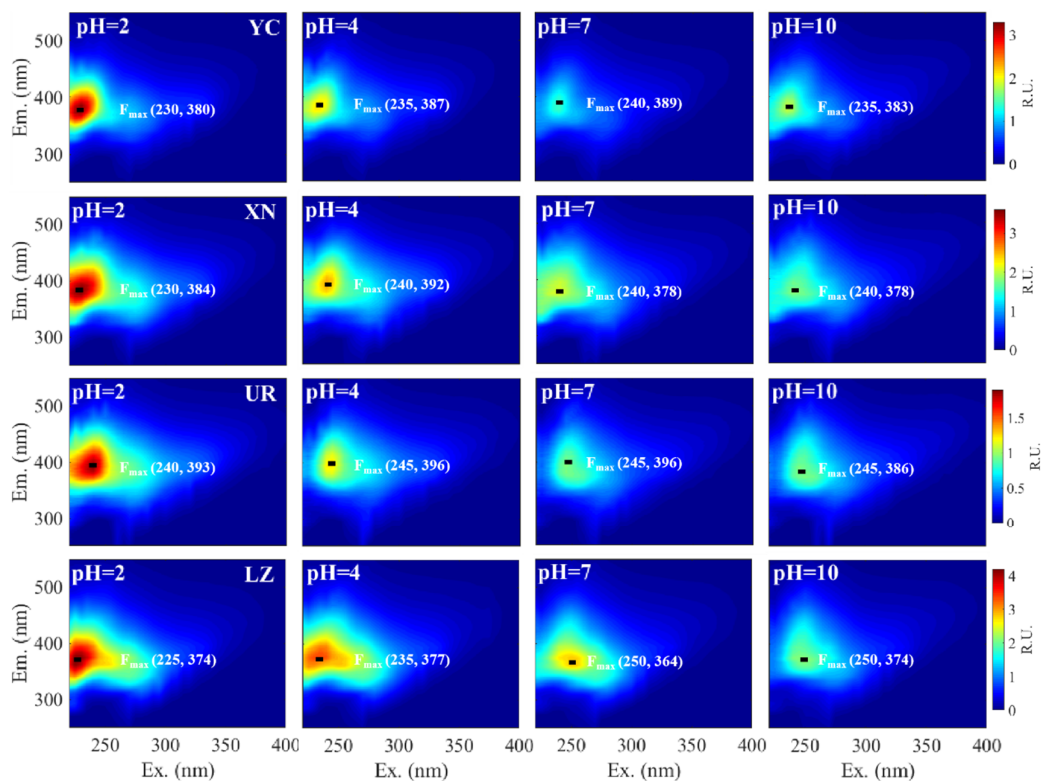
Figure 6. EEM spectra and the fluorescence peak (Ex, Em) of WSOA at different pH values in four cities.
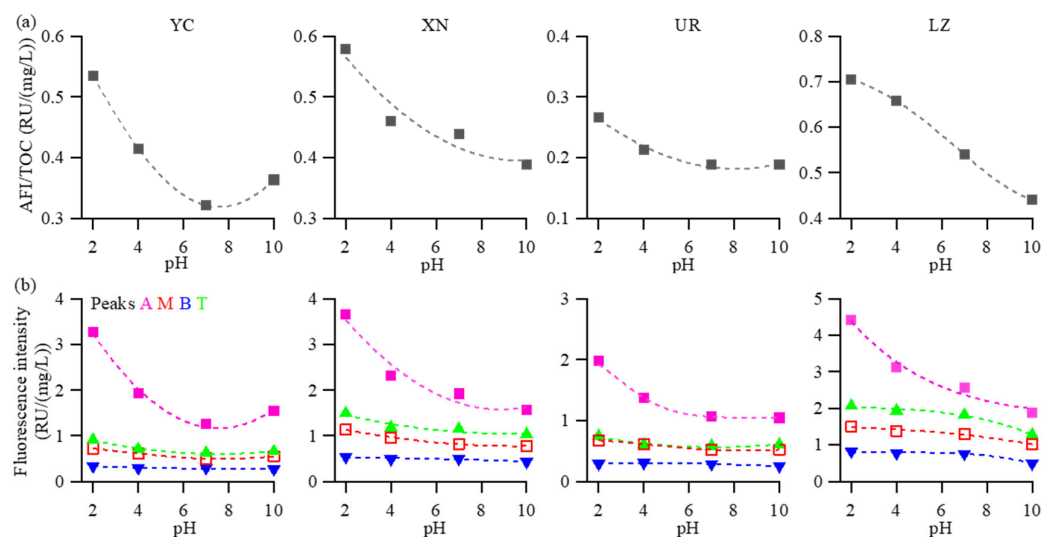
Figure 7. (a) The AFI/TOC and (b) maximum peak intensity of major fluorescence peaks as a function of pH values.
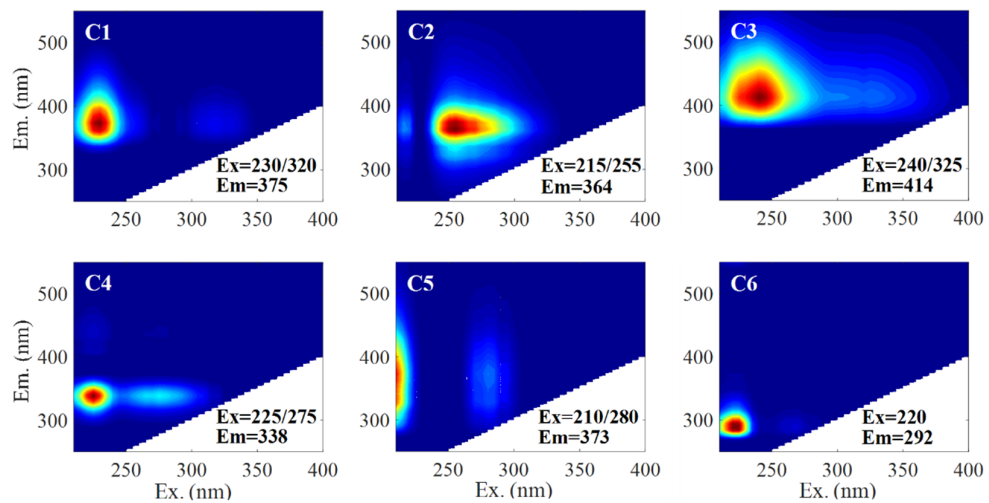
Figure 8. The EEM components identified by the PARAFAC model for the WSOA.
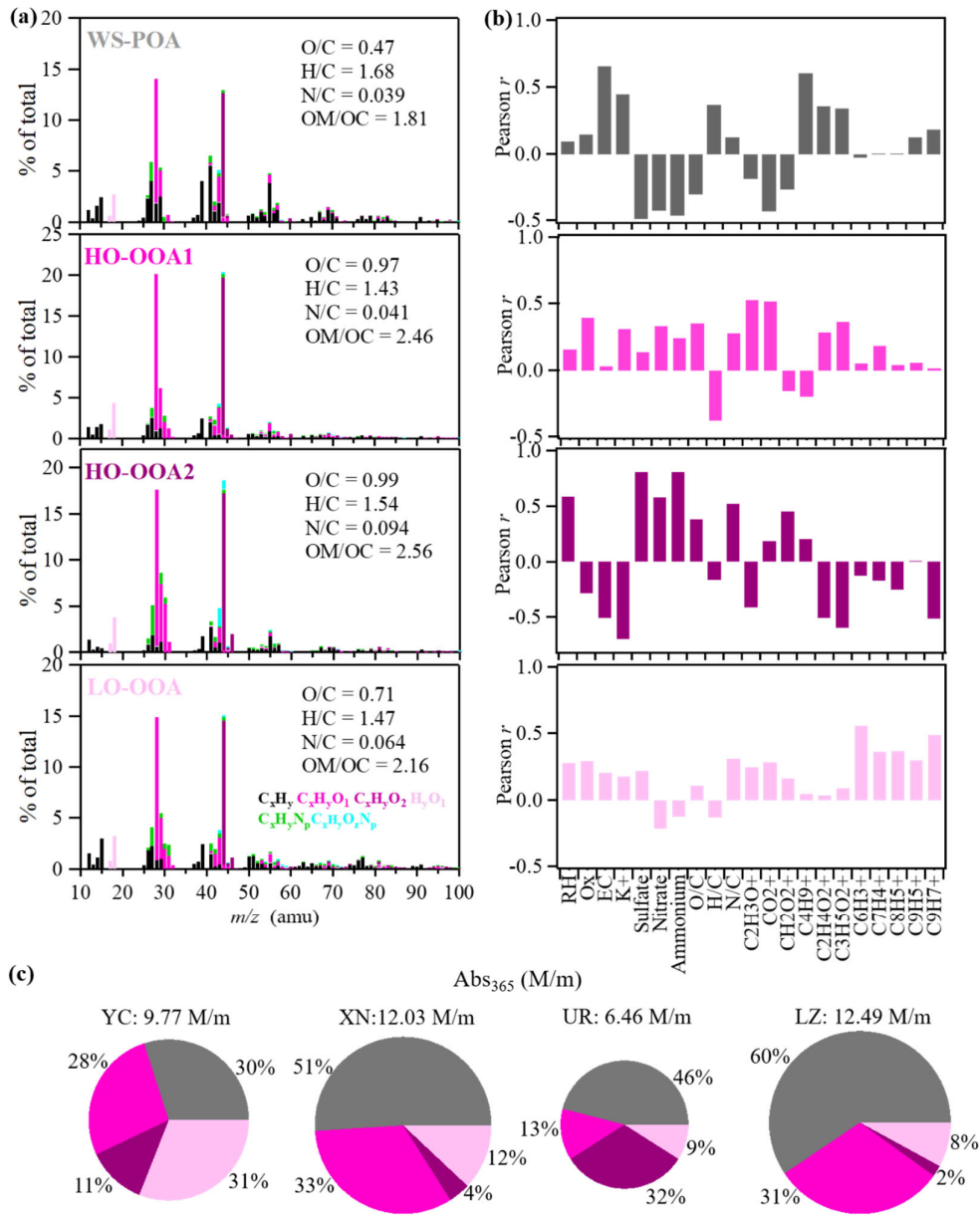
Figure 9. (a) The mass spectra of PMF factors (WS-POA, HO-OOA1, HO-OOA2, LO-OOA), (b) correlations between PMF factors and various tracers, and (c) average contributions of WSOA factors to light absorption at 365 nm.
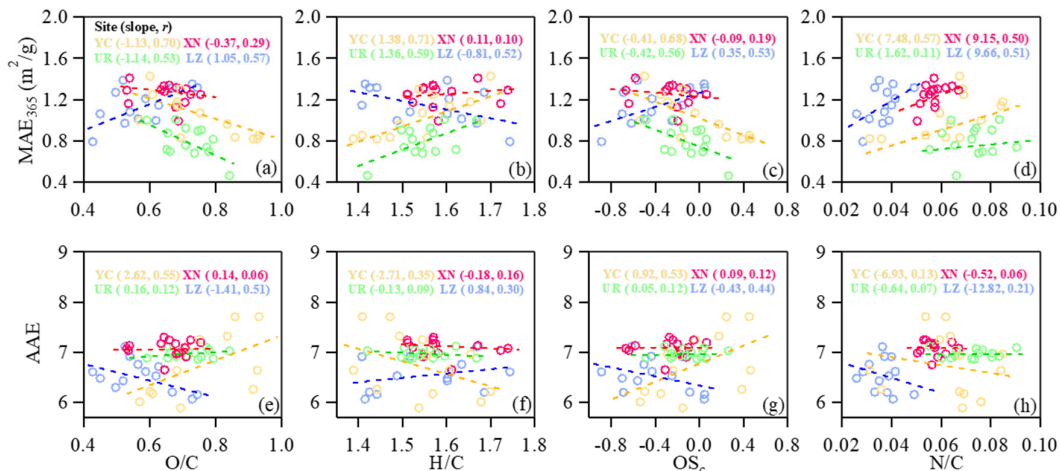
Figure 10. Scatter plots of MAE$_{365}$ (a–d) and AAE (e–h) vs. (a, e) O/C, (b, f) H/C, (c, g) OS$_c$, and (d, h) N/C in four cities. The slope and correlation coefficient ® by fitting the scatter of each group are shown, and p-test is significant at the 0.05 level when r reached 0.49.
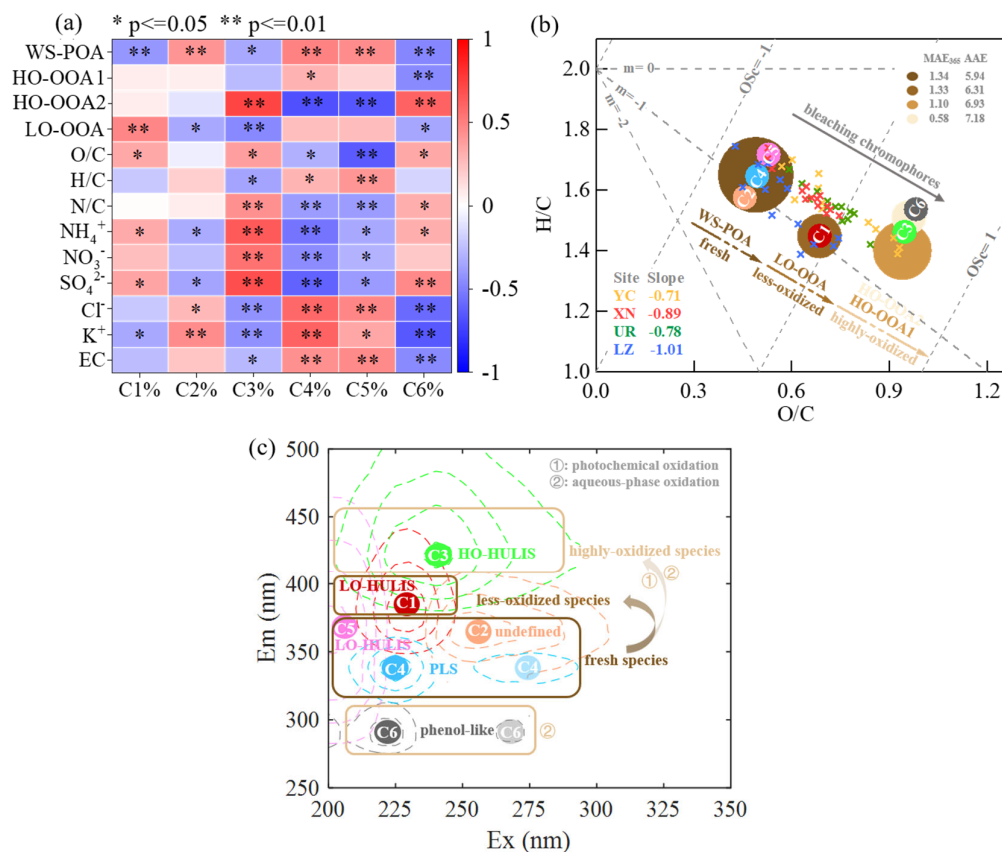
Figure 11. The diagram illustrates the aging from fresh species to less oxidized and/or highly-oxidized species and corresponding variation on optical properties. (a) Heatmap of the correlation analysis between the PARAFAC components and PMF factors, with highly significant correlations (p < 0.01) are marked by** and significant correlations (0.01 < p < 0.05) marked by *. (b) The Van Krevelen plot (H:C vs. O:C) for ambient WSOA samples and different WSOA factors in this study,

with the slopes of the fitted line for ambient WSOA samples from each city noted in the lower left. The fitted MAE_{365} and AAE values for each WSOA factor are noted in the upper right, and each WSOA factor is colored by its MAE_{365} value, with fading color indicating bleaching chromophores. The size of the color block represents the average contribution of each WSOA factor to Abs_{365}. Based on the correlation coefficients between PARAFAC components and PMF factors, C2, C4, and C5 chromophores were assigned to WS-POA, C1 chromophore assigned to LO-OOA, and C3 and C6 chromophore assigned to HO-OOA (HO-OOA1 and HO-OOA2). (c) The Ex-Em plot for fluorescence peak positions (Ex/Em) and the corresponding compounds of these six fluorophores.

Tables

Table 1. Light-absorbing properties of BrC in $PM_{2.5}$ water extract in four cities.

Light absorption property	YC	XN	UR	LZ
AAE	6.81 ± 0.69	7.06 ± 0.44	6.94 ± 0.25	6.41 ± 0.51
Abs_{365} (M/m)	9.77 ± 4.74	12.03 ± 3.16	6.46 ± 1.60	12.49 ± 4.94
MAE_{365} (m^2/g)	1.02 ± 0.23	1.22 ± 0.18	0.78 ± 0.16	1.19 ± 0.12
k_{365}	0.041 ± 0.007	0.049 ± 0.005	0.034 ± 0.006	0.046 ± 0.008
$SFE_{300-700}$ (W/g)	3.72 ± 0.90	4.42 ± 0.72	2.97 ± 0.67	4.35 ± 1.01